WSM WORLD STRESS MAP

WSM Technical Report 16-01

WSM quality ranking scheme, database description and analysis guidelines for stress indicator

Oliver Heidbach, Andreas Barth, Birgit Müller, John Reinecker
Ove Stephansson, Mark Tingay, Arno Zang

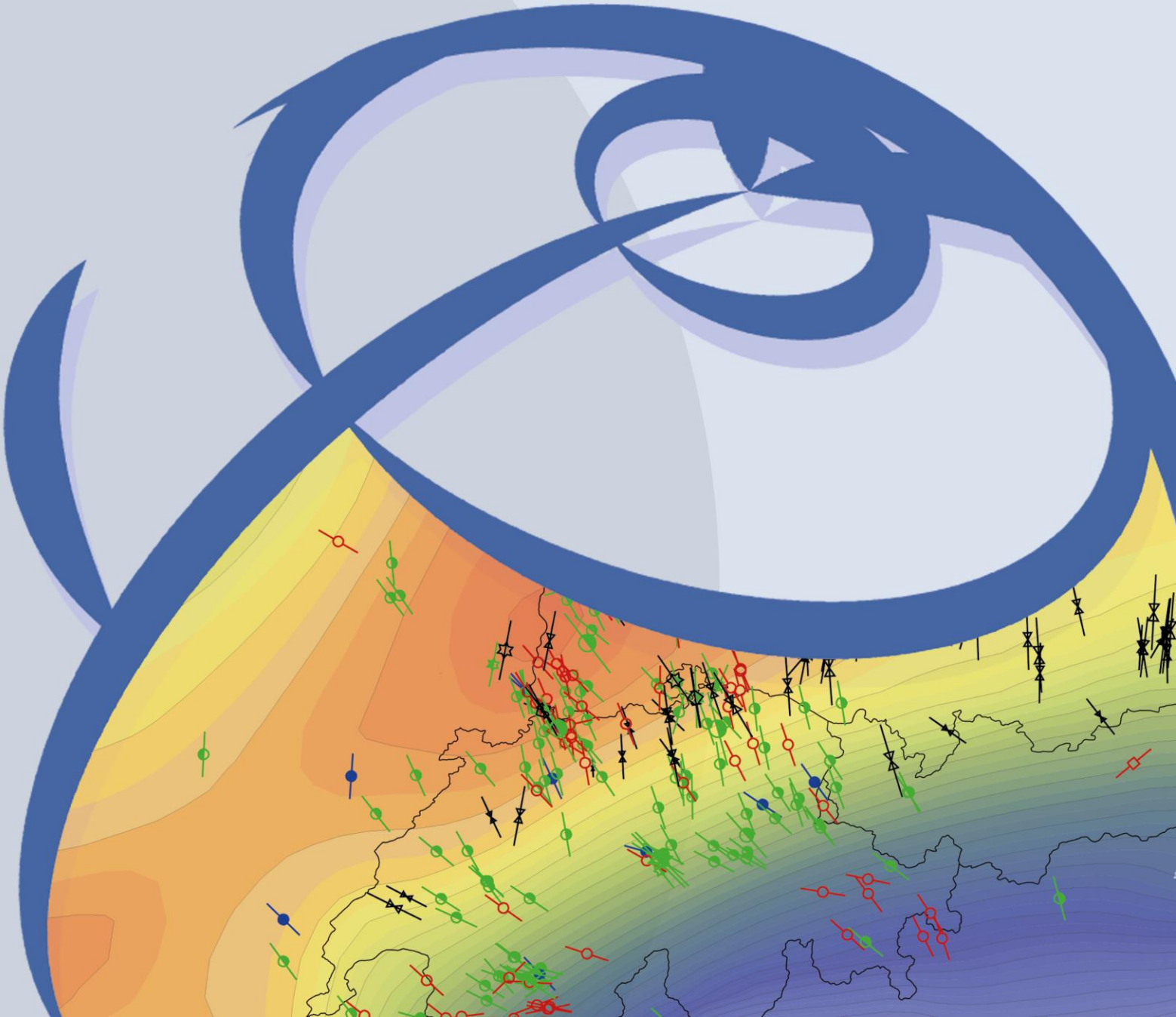

Recommended citation of the report:

Heidbach, O.; Barth, A.; Müller, B.; Reinecker, J.; Stephansson, O.; Tingay, M.; Zang, A. (2016). WSM quality ranking scheme, database description and analysis guidelines for stress indicator. World Stress Map Technical Report 16-01, GFZ German Research Centre for Geosciences.
DOI: http://doi.org/10.2312/wsm.2016.001

The World Stress Map Database Release 2016 is published as:

Heidbach, O.; Rajabi, M.; Reiter, K.; Ziegler, M. and the WSM Team (2016): World Stress Map Database Release 2016. GFZ Data Services. http://doi.org/10.5880/WSM.2016.001

The following stress maps are available (to be continued)

Heidbach, O., Rajabi, M., Reiter, K., & Ziegler, M. (2016). ***World Stress Map 2016*** [Dataset]. GFZ Data Services. https://doi.org/10.5880/WSM.2016.002

Heidbach, O., Custodio, S., Kingdon, A., Mariucci, M. T., Montone, P., Müller, B.; Pierdominici, S.; Rajabi, M.; Reinecker, J.; Reiter, K.; Tingay, M.; Williams, J.; Ziegler, M. (2016***). Stress Map of the Mediterranean and Central Europe 2016*** [Dataset]. GFZ Data Services. https://doi.org/10.5880/WSM.EUROPE2016

Reiter, K., Heidbach, O., Müller, B., Reinecker, J., & Röckel, T. (2016). ***Spannungskarte Deutschland 2016*** [Dataset]. GFZ Data Services. https://doi.org/10.5880/WSM.GERMANY2016

Reiter, K., Heidbach, O., Müller, B., Reinecker, J., & Röckel, T. (2016). ***Stress Map Germany 2016*** [Dataset]. GFZ Data Services. https://doi.org/10.5880/WSM.GERMANY2016_EN

Ziegler, M., Rajabi, M., Hersir, G., Ágústsson, K., Árnadóttir, S., Zang, A.; Bruhn, D.; Heidbach, O. (2016). Stress Map Iceland 2016 [Data set]. GFZ Data Services. https://doi.org/10.5880/WSM.ICELAND2016

Imprint

World Stress Map Project
GFZ German Research Centre for Geosciences

Telegrafenberg
D-14473 Potsdam
Published in Potsdam, Germany
September 2016
http://doi.org/10.2312/wsm.2016.001

WSM Technical Report 16-01

WSM quality ranking scheme, database description and analysis guidelines for stress indicator

Oliver Heidbach, Andreas Barth, Birgit Müller, John Reinecker,
Ove Stephansson, Mark Tingay, Arno Zang
GFZ German Research Centre for Geosciences, Potsdam, Germany

GFZ
Helmholtz Centre
POTSDAM

Table of Contents

List of Tables

List of Figures

1 Introduction

1.1 Overview

The World Stress Map (WSM) compiles information of the contemporary crustal stress using a wide range of very different stress indicator which can be grouped into four categories:

- Earthquake focal mechanisms
- Well bore breakouts and drilling-induced fractures
- In-situ stress measurements (overcoring, hydraulic fracturing, borehole slotter)
- Young geologic data (from fault-slip analysis and volcanic vent alignments)

A detailed description of the stress indicator in the context of the WSM project can be found in Zoback and Zoback [1991], Zoback et al. (1989), Zoback and Zoback [1980], and Sperner et al. [2003]. A more general overview of tectonic stress and stress indicator can be found in review publications and standard text book [*Bell*, 1996; *Engelder*, 1992; *Jaeger et al.*, 2007; *Ljunggren et al.*, 2003; *Schmitt et al.*, 2012; *Zang and Stephansson*, 2010; *Zoback*, 2010; Zoback, 1992]. An alternative grouping of the stress indicator using a technical perspective is presented in Fig. 1.1-1

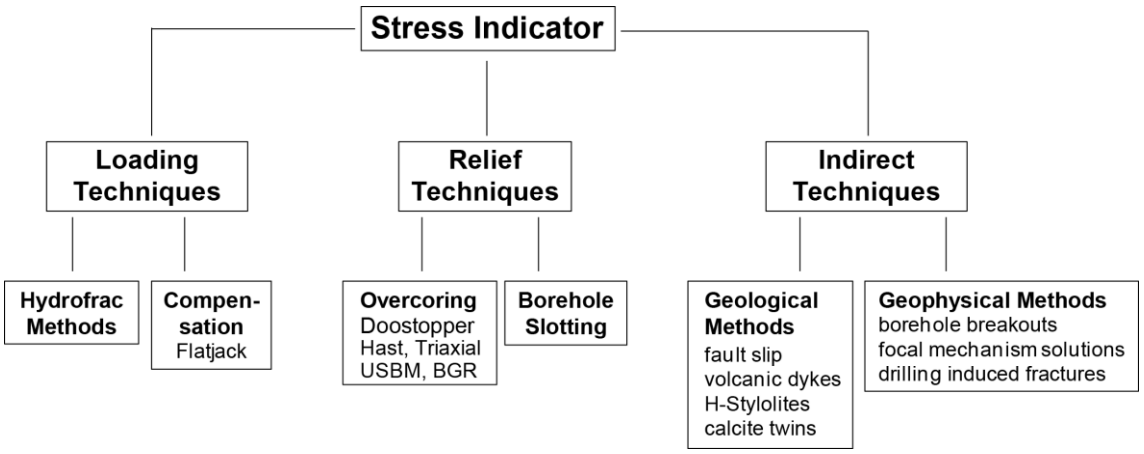

Fig. 1.1-1: Technical classification of the different stress indicator.

Details on individual stress indicator are presented in the above mentioned literature and the analysis guidelines presented in chapters 3-6.

The stress state is described with the nine components of the stress tensor σ_{ij}, but due to the symmetry properties of the stress tensor ($\sigma_{ij} = \sigma_{ji}$ for $i \neq j$) only six components are independent from each other (Fig. 1.2-1). Thus the stress state can always be transformed in a principal axis coordinate system (right). Then the three orientations and three magnitudes of the principal stresses σ_1, σ_2 and σ_3 describe the stress state. Assuming that in the Earth crust one of principal stresses is the vertical stress S_V which is the overburden, the orientation of the stress tensor is given by the orientation of one of the two horizontal

stresses S_{Hmax} and S_{hmin} which are the maximum and minimum horizontal stress, respectively. All stress indicator used for the WSM provide at least the S_{Hmax} orientation which is visualized in the stress maps.

This report presents and explains technical details of the WSM database release 2016 [*Heidbach et al.*, 2016b] visualized with the World Stress Map 2016 (Fig. 1.1-1). Chapter 2 explains the basics and concept of the WSM quality ranking scheme, the stress regime assignment and the procedure of the assignment of the possible plate boundary label to some of the data records that are derived from single focal mechanism solutions. Chapter 3-6 presents the WSM analysis guidelines of the most common stress indicator and chapter 7 gives the detailed explanation of each field of the data records in the WSM database.

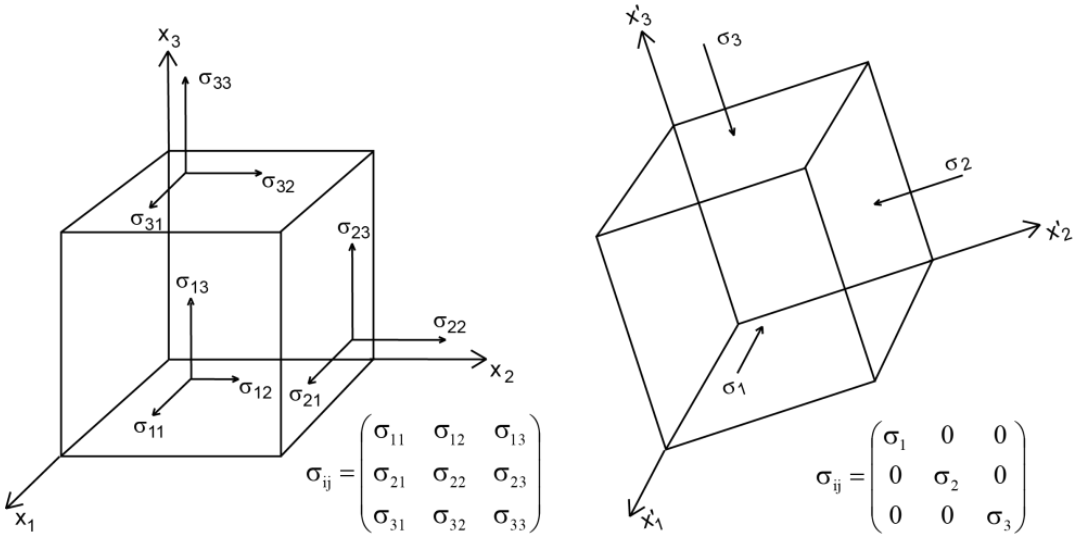

Fig. 1.1-1: Components of the stress tensor σ_{ij} and principal stresses.

The stress state is described with the nine components of the stress tensor σ_{ij} (left). Due to the symmetry properties ($\sigma_{ij} = \sigma_{ji}$ for $i \neq j$) only six components are independent from each other and thus the stress state can always be transformed in a principal axis coordinate system (right). Then the three orientations and three magnitudes of the principal stresses σ_1, σ_2 and σ_3 describe the stress state.

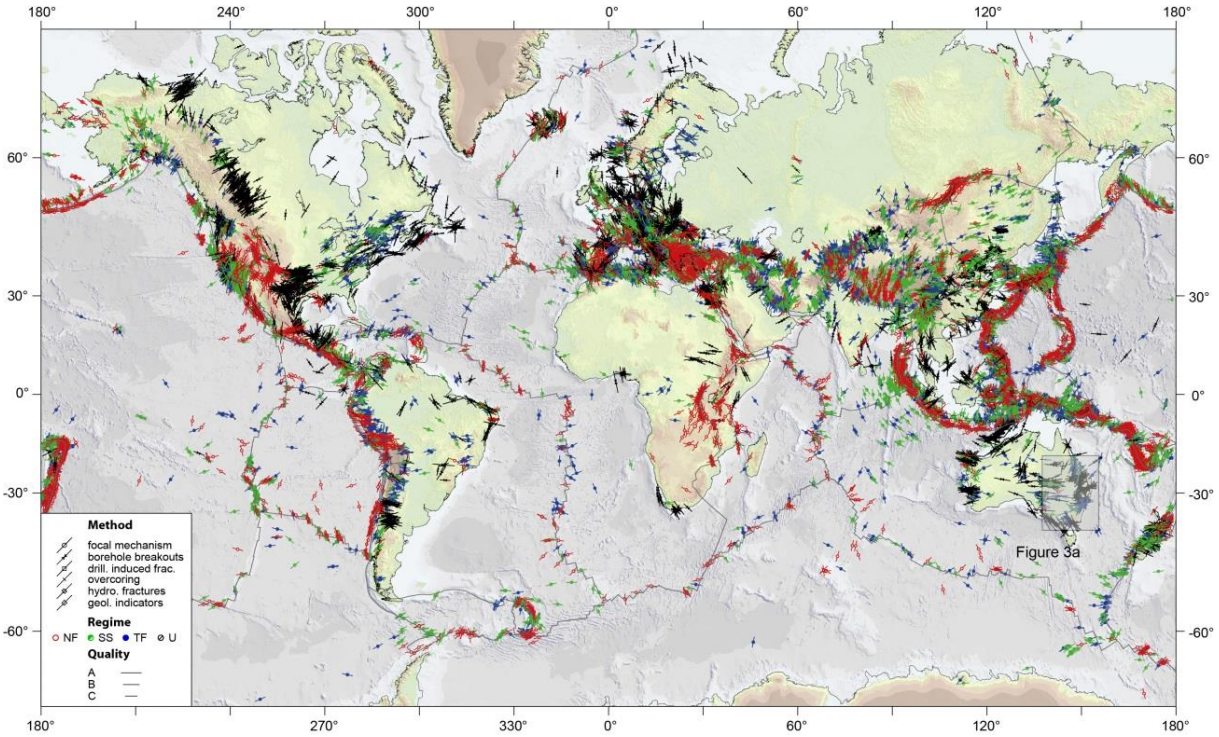

Fig. 1.2-1: World Stress Map 2016.

Displayed are A-C quality data records of the WSM database release 2016 ([*Heidbach et al.*, 2016a; *Heidbach et al.*, 2016b]). Lines show the orientation of S_{Hmax} and the symbols denote the stress indicator type. Colours indicate stress regimes with red for normal faulting (NF), green for strike-slip faulting (SS), blue for thrust faulting (TF), and black for unknown regime (U). Data from focal mechanism solutions with A-C quality that are labelled as possible plate boundary events are not displayed.

1.2 Stress term definitions

In geoscientific and rock engineering literature there is no strict agreement on stress term definitions. Thus, a brief description is given on how stress terms are used in this report. Beyond these definitions we point out that in this study compression is positive in contrast to engineering convention where compression has a negative sign.

Tab. 1.2-1: Definition of stress terms.

Due to the fact that there is no strict definition of stress terms in the literature [e.g. *Engelder*, 1992; *Engelder*, 1994; *Jaeger et al.*, 2007; *Zang and Stephansson*, 2010; *M Zoback*, 2010], a brief definition of the stress terms used in this report is given.

Term	Symbol	Definition/Comment
in-situ stress state	-	Undisturbed natural stress state; also called virgin stress state. In particular the in situ stress is the sum of all natural stress contributions and natural processes that influence rock stress state at a given point.
disturbed in-situ stress state	-	Denotes that the in situ stress is disturbed due to man-made changes in the underground or loads on the surface such as impoundment, drilling, tunnelling, mining, fluid stimulation, reservoir depletion, re-injection of waste water to name a few.

Term	Symbol	Definition/Comment
principal stresses	σ_1, σ_2, σ_3 (S1, S2, S3)	The symmetric stress tensor can always be transformed into a principal axes system [*Jaeger et al.*, 2007]. The three remaining non-zero components in the diagonal of the matrix are the principal stresses where σ_1 is the largest and σ_3 the smallest ($\sigma_1 \geq \sigma_2 \geq \sigma_3$). Often S1, S2 and S3 are used alternatively to denote the three principal stresses.
differential stress	$\sigma_d=\sigma_1-\sigma_3$	Difference between the largest and the smallest principal stress.
effective stresses	σ‘	Effective stresses σ‘ are total stresses σ minus pore fluid pressure p_f.
vertical stress	S_V	The magnitude of S_v is the integral of the overburden. Only at the Earth surface S_V is one of the principal stresses; at greater depth S_V can deviate from a principal stress orientation.
Orientation of the maximum and minimum horizontal stress	S_{Hmax}, S_{hmin}	Assuming that the vertical stress S_v is a principal stress at depth S_H und S_h are the other two principal stresses of the stress tensor. Otherwise S_{Hmax} and S_{hmin} are the projections of the principal stresses into the horizontal plane.
stress regime	-	Relates to stresses: The stress regime is an expression of the relative magnitudes of the principal stresses. It can be expressed as a continuous value using the Regime Stress Ratio (RSR) with values between 0 and 3 [*Simpson*, 1997].
stress pattern	-	Spatial uniformity or variability of a certain aspect of the stress tensor e.g. the pattern of the S_H orientation [*Heidbach et al.*, 2007; *Heidbach et al.*, 2010; *Hillis and Reynolds*, 2000; *M. L. Zoback*, 1992].
transient stresses	-	The far-field forces due to plate tectonics are constant over long distances (> 1000 km) and long-time scales (> 100 ka). However, close to active tectonics the stress state is perturbed locally within the seismic cycle and thus changes constantly. Also in areas with low viscosity or overpressured fluids close to lithostatic pressure the stress state can be transient due to short relaxation times or creep processes.
tectonic stresses	-	According to Engelder [1992] tectonic stresses are the horizontal components of the in situ stress state that deviate from a given reference stress state (e.g. uniaxial, lithostatic). In particular a reference stress state implies that the magnitudes of S_{Hmax} and S_{hmin} are equal. However, definitions in the literature are not consistent. Tectonic stress must not necessarily equal the deviatoric stress which is the non-isotropic part of the stress tensor (the isotropic part is the mean stress σ_m or one third of the trace of the of stress tensor $\sigma_m = 1/3(\sigma_{11}+\sigma_{22}+\sigma_{33}) = 1/3(\sigma_1+\sigma_2+\sigma_3)$. This is only true when one assumes that the reference stress state is lithostatic ($S_{Hmax}=S_{hmin}=S_v$ with the assumption that S_V is a principal stress).
remnant/ residual stresses	-	Due to high viscosity of the upper crust the response to any kind of load is mainly elastic with high relaxation times of tectonic stresses in the order of tens or hundreds of million years. Thus the stresses due to past geological processes can be stored over very long time spans and are called residual or remanent stresses [*Friedmann*, 1972; *McGarr and Gay*, 1978; *Zang and Stephansson*, 2010].
tectonic regime	-	Relates to fault kinematics: Thrust faulting, normal faulting and strike-slip after Anderson [1905]. Only when faults are optimally oriented in the stress field the stress regime is coincident with the tectonic regime [*Célérier*, 1995; *Célérier et al.*, 2012; *Hergert and Heidbach*, 2011]. Normal faulting: $S_v > S_{Hmax} > S_{hmin}$; Thrust faulting: $S_{Hmax} > S_{hmin} > S_v$; Strike-slip: $S_{Hmax} > S_v > S_{hmin}$

1.3 References

Anderson, E. M. (1905), The dynamics of faulting, Trans. Edin. Geol. Soc., 8, 387-402.

Bell, J. S. (1996), In situ stresses in sedimentary rocks (Part 1): measurement techniques, Geoscience Canada, 23, 85-100.

Célérier, B. (1995), Tectonic regime and slip orientation of reactivated faults, Geophys. J. Int., 121, 143-161.

Célérier, B., A. Etchecopar, F. Bergerat, P. Vergely, F. Arthaud, and P. Laurent (2012), Inferring stress from faulting: From early concepts to inverse methods Tectonophys., doi: 10.1016/j.tecto.2012.1002.1009 1206-1219.

Engelder, T. (1992), Stress Regimes in the Lithosphere, 457 pp., Princeton, NJ.

Engelder, T. (1994), Deviatoric Stressitis: A Virus Infecting the Earth Science Community, EOS Trans., 75, 209, 211-212.

Friedmann, M. (1972), Residual elastic strain in rocks, Tectonophys., 15, 297-330.

Heidbach, O., M. Rajabi, K. Reiter, and M. Ziegler (2016a), World Stress Map 2016, edited by G. D. Services, GFZ German Research Centre for Geosciences, doi:10.5880/WSM.2016.002.

Heidbach, O., M. Rajabi, K. Reiter, M. Ziegler, and a. t. W. Team (2016b), World Stress Map Database Release 2016, edited by G. D. Services, GFZ German Research Centre for Geosciences, doi:10.5880/WSM.2016.001.

Heidbach, O., J. Reinecker, M. Tingay, B. Müller, B. Sperner, K. Fuchs, and F. Wenzel (2007), Plate boundary forces are not enough: Second- and third-order stress patterns highlighted in the World Stress Map database, Tectonics, 26, TC6014, doi:10.1029/2007TC002133.

Heidbach, O., M. Tingay, A. Barth, J. Reinecker, D. Kurfeß, and B. Müller (2010), Global crustal stress pattern based on the World Stress Map database release 2008, Tectonophys., 482, 3-15, doi:10.1016/j.tecto.2009.07.023.

Hergert, T., and O. Heidbach (2011), Geomechanical model of the Marmara Sea region - II. 3-D contemporary background stress field, Geophys. J. Int., doi:10.1111/j.1365-1246X.2011.04992.x, 01090-01102.

Hillis, R. R., and S. D. Reynolds (2000), The Australian Stress Map, J. Geol. Soc., 157, 915-921.

Jaeger, J. C., N. G. W. Cook, and R. W. Zimmermann (2007), Fundamentals of Rock Mechanics, 4th ed., Blackwell Publishing, Oxford.

Ljunggren, C., Y. Chang, T. Janson, and R. Christiansson (2003), An overview of rock stress measurement methods, Int. J. Rock. Mech., 40, 975-989.

McGarr, A., and N. C. Gay (1978), State of Stress in the Earth's Crust, Ann. Rev. Earth Planet. Sci., 6, 405-436.

Schmitt, D. R., C. A. Currie, and L. Zhang (2012), Crustal stress determination from boreholes and rock cores: Fundamental principles Tectonophys., doi: 10.1016/j.tecto.2012.1008.1029 1011-1026.

Simpson, R. W. (1997), Quantifying Anderson's fault types, J. Geophys. Res., 102, 17909-17919.

Sperner, B., B. Müller, O. Heidbach, D. Delvaux, J. Reinecker, and K. Fuchs (2003), Tectonic stress in the Earth's crust: advances in the World Stress Map project, in New insights in structural interpretation and modelling, edited by D. A. Nieuwland, pp. 101-116, Geological Society, London.

Zang, A., and O. Stephansson (2010), Stress in the Earth's Crust, 1st ed., 323 pp., Springer, Heidelberg.

Zoback, M. (2010), Reservoir Geomechanics, 2nd edition ed., 449 pp., Cambridge, Cambridge.

Zoback, M., and M. L. Zoback (1991), Tectonic stress field of North America and relative plate motions, in Neotectonics of North America, edited by D. B. Slemmons, E. R. Engdahl, M. D. Zoback and D. D. Blackwell, pp. 339-366, Geological Society of America, Boulder, Colorado.

Zoback, M. L. (1992), First and second order patterns of stress in the lithosphere: The World Stress Map Project, J. Geophys. Res., 97, 11703-11728.

Zoback, M. L., and M. Zoback (1980), State of Stress in the Conterminous United States, J. Geophys. Res., 85(B11), 6113-6156.

Zoback, M. L., and M. Zoback (1989), Tectonic stress field of the conterminous United States, in Geophysical Framework of the Continental United States, edited by L. C. Pakiser and W. D. Mooney, pp. 523-539, Geol. Soc. Am. Mem., Boulder, Colorado.

2 WSM quality ranking scheme and stress regime assignment

2.1 Introduction

The success of the WSM is based on a standardized the quality ranking scheme for the individual stress indicators making them comparable on a global scale. The ranking scheme is based mainly on the number, the accuracy, and the depth of the measurements. The quality ranking scheme was introduced by Zoback and Zoback [1991; 1989] and refined and extended by Sperner et al. [2003] and Heidbach et al. [2010]. It is internationally accepted and guarantees reliability and global comparability of the stress data. The current WSM database release 2016 uses the quality ranking scheme Version 2008. Note that the quality ranking scheme is set up to combine a stress data that come from very different stress indicator representing very different rock volumes.

2.2 The WSM quality ranking scheme

Each stress data record is assigned a quality between A and E, with A being the highest quality and E the lowest (Tab. 2.2-1). A quality means that the orientation of the maximum horizontal compressional stress S_{Hmax} is accurate to within ±15°, B quality to within ±20°, C quality to within ±25°, and D quality to within ±40°. For the most methods these quality classes are defined through the standard deviation of S_{Hmax}. E-quality data records do not provide sufficient information or have standard deviations greater than 40°. These data records are mainly for well bores, contain no stress information, but are only kept for book keeping purposes that these data have been processed. In general, A-, B- and C-quality stress indicators are considered reliable for the use in analyzing stress patterns and the interpretation of geodynamic processes.

Tab. 2.2-1: WSM quality ranking scheme.

The abbreviation s.d. stands for standard deviaion.

Stress indicator		A S_H believed to be within ± 15°	B S_H believed to be within ± 15-20°	C S_H believed to be within ± 20-25°	D Questionable S_H orientation (± 25-40°)	E no reliable information (> ± 40°)
Focal Mechanism (FM)	**Formal Inversion (FMF)**	• Formal inversion of ≥ 15 well constrained single event solutions in close geographic proximity and s.d. or misfit angle ≤ 12°	• Formal inversion of ≥ 8 well constrained single event solutions in close geographic proximity and s.d. or misfit angle ≤ 20°	-	-	-
	Single (FMS)	-	-	• Well constrained single event solution, M ≥ 2.5 (e.g. CMT solutions)	• Well constrained single event solution, M < 2.5	• Mechanism with P,B,T axes all plunging 25°-40° • Mechanism with P and T axes both plunging 40°-50°
	Average (FMA)	-	-	-	• Average of P-axis trends or circular statistics of P-axis trends • Composite solutions	
Borehole Breakout (BO)	from caliper logs	• ≥ 10 distinct breakout and combined length ≥ 300 m in a single well with s.d. ≤ 12°	• ≥ 6 distinct breakout and combined length ≥ 100 m in a single well with s.d. ≤ 20°	• ≥ 4 distinct breakouts and combined length ≥ 30 m with s.d. ≤ 25°	• < 4 distinct breakouts or < 30 m combined length in a single well with s.d. ≤ 40°	• Wells without reliable breakouts or s.d. > 40°
	from image logs	• ≥ 10 distinct breakout zones and combined length ≥ 100 m in a single well with s.d. ≤ 12°	• ≥ 6 distinct breakout zones and combined length ≥ 40 m in a single well with s.d. ≤ 20°	• ≥ 4 distinct breakouts and combined length ≥ 20 m with s.d. ≤ 25°	• < 4 distinct breakouts or < 20 m combined length in a single well with s.d. ≤ 40°	
Drilling Induced Fractures (DIF)		• ≥ 10 distinct fracture zones in a single well with a combined length ≥ 100 m and s.d. ≤ 12°	• ≥ 6 distinct fracture zones in a single well with a combined length ≥ 40 m and s.d. ≤ 20°	• ≥ 4 distinct fracture zones in a single well with a combined length ≥ 20 m and s.d. ≤ 25°	• < 4 distinct fracture zones in a single well or a combined length < 20 m and s.d. ≤ 40°	• Wells without fracture zones or s.d. > 40°
Hydraulic Fracture (HF)		• ≥ 5 hydrofrac orientations in a single well with s.d. ≤ 12° • depth ≥ 300 m, and distributed over a depth range ≥ 300 m	• ≥ 4 hydrofrac orientations in a single well with s.d. ≤ 20° • depth ≥ 100 m, and distributed over a depth range ≥ 200 m	• ≥ 3 hydrofrac orientations in a single well with s.d. ≤ 25° • depth ≥ 30 m, and distributed over a depth range ≥ 100 m	• Single hydrofrac orientation	• Wells in which only stress magnitudes are measured, without information on orientations
Overcoring (OC) and **Borehole Slotter (BS)**		• ≥ 11 measurements with depth ≥ 300 m and s.d. ≤ 12°	• ≥ 8 measurements with depth ≥ 100 m and s.d. ≤ 20°	• ≥ 5 measurements with depth ≥ 30 m and s.d. ≤ 25°	• ≥ 2 measurements with depth ≥ 10 m and s.d. ≤ 40°	• < 2 measurements or depth < 10 m or s.d. > 40° • Measurements in boreholes extending less than two excavation radii from the excavation wall • Distance to topographic features less than three times the height of the topographic feature
Fault Slip (GF)		• Inversion of ≥ 25 fault-slip data with a fluctuation ≤ 9° for ≥ 60% of the whole dataset	• Inversion of ≥ 15 fault-slip data with a fluctuation ≤ 12° for ≥ 45% of the whole dataset	• Inversion of ≥ 10 fault-slip data with a fluctuation ≤ 15° for ≥ 30% of the whole dataset • Attitude of fault and primary sense of slip known, no actual slip vector	• Inversion of ≥ 6 fault-slip data with a fluctuation ≤ 18° for ≥ 15% of the whole dataset • Offset core holes • Quarry popups • Postglacial surface fault offsets	-
Volcanic Vent Alignment (GVA)		• ≥ 5 Quaternary vent alignments or "parallel" dikes with s.d. ≤ 12°	• ≥ 3 Quaternary vent alignments or "parallel" dikes with s.d. ≤ 20°	• Single well-exposed Quaternary dike • Single alignment with ≥ 5 vents	• Volcanic alignment inferred from < 5 vents	-
Petal Centerline Fractures (PC)		-	-	• Mean orientation of fractures in a single well with s.d. ≤ 20°	-	-

2.3 Stress regime assignment

From the stress indicators which provide absolute or relative stress magnitudes the tectonic regime is derived according to the stress regime categorization table. The stress magnitudes are defined using the standard geologic/geophysical notation with compressive stress positive and S1>S2>S3, so that S1 is the maximum and S3 the minimum principal stress.

Besides the standard NF, TF, and SS categories, combinations of NF with SS (NS) and TF with SS (TS) exist (Zoback, 1992). NS represents data where the maximum principal stress or P-axis is the steeper plunging of the P- and B-axes. TS represent data where the minimum principal stress or T-axis is the steeper plunging of the B- and T-axes. The plunges (pl) of P-, B-, and T-axes (or S1, S2, and S3 axes) used to assign the stress data to the appropriate stress regime are given in the table below (according to Zoback, 1992).

For some overcoring (OC) and hydraulic testing of pre-existing fractures (HFG) measurements, the magnitudes of the full stress tensor are determined and the S_{Hmax} azimuth can be calculated directly from the eigenvectors of the tensor. However, the stress regime characterization is still based on the plunges of the principal axes.

The exact cutoff values defining the stress regime categories are subjective. In this attempt Zoback (1992) used the broadest possible categorization consistent with actual P-, B-, and T-axes values. The choice of axes used to infer the maximum horizontal stress (S_{Hmax}) orientation is displayed in the table above, e.g. the S_{Hmax} orientation is taken as the azimuth of the B-axis in case of a pure normal faulting regime (NF) and as 90° + T-axis azimuth in the NS case when the B-axis generally plunges more steeply than the T-axis.

If data fall outside of the ranges the tectonic regime cannot be assigned. When the focal mechanism comes from the routine analysis of the Global CMT catalogue the data record will not be entered into the database. If the focal mechanism comes from a regional study it is given an E-quality and unkown tectonic regime (U). E.g. this holds on in particular for focal mechanism all three axes have moderate plunges (between 25° and 45°) and when both P- and T-axes have nearly identical plunges in the range of 40° to 50°.

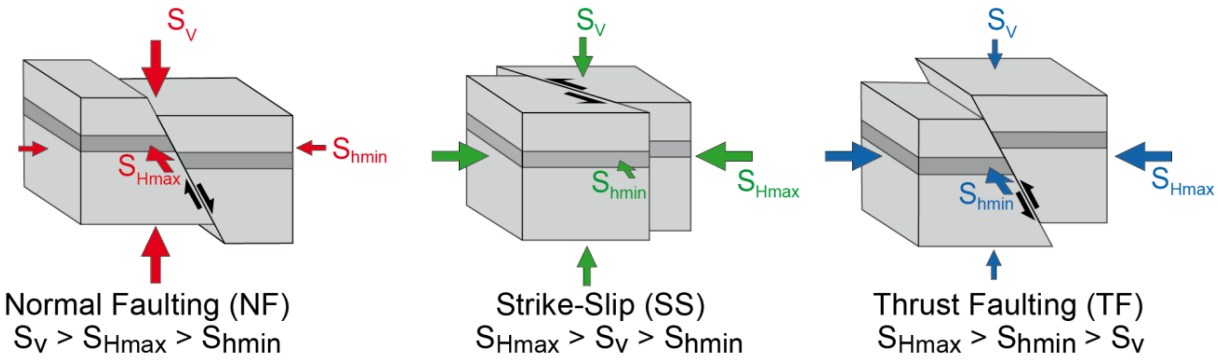

Fig. 2.3-1: The three main tectonic stress regimes.

Left: S_H orientation at the middle surface of the Opalinus Clay as contour plot and lines. Lines and symbols show the S_{Hmax} orientation from the new stress compilation in Switzerland. Thin lines show the location of the cross sections. Right top: S_{Hmax} orientation on an EW cross sections. Right bottom: S_{Hmax} orientation on a NS cross sections. Thin lines denote location of the profiles and the top and bottom of the Opalinus Clay.

2.4 Assignment of the Possible Plate Boundary (PBE) label

Plate boundaries are characterized by faults with preferred orientations and presumably include major faults with a low coefficient of friction which can be easily reactivated. Thus, the derivation of stress orientations from a single focal mechanism is not always an unambiguous matter, because of its dependence on the mechanical behaviour of the involved fault zone. In the case of weak faults the angle between the principal stress axes S1, S2, and S3 and the principal strain axis P, B, and T from the moment tensor might be as large as 90° [*McKenzie*, 1969]. The scientific debate about the strength of plate boundary faults - whether they are weak or strong - is still going on [e.g. *Provost et al.*, 2003]. Users should be aware that stress orientations derived from single focal mechanism solutions (FMS) along weak plate boundaries might have a higher degree of uncertainty.

Although it is beyond the objectives of the WSM project to take part in such debates, it is the role of the WSM to provide its users with stress data that have been reliably quality controlled. To this end, FMS data records located near plate boundaries have been flagged as Possible Plate Boundary Events (PBE) if they meet the following criteria:

1. The event is located within a critical horizontal distance relative to the closest plate boundary segment. The critical distances depend on the types of plate boundaries. We estimated them by means of statistical analysis as being 45 km for continental transform faults, 80 km for oceanic transform faults, 70 km for oceanic spreading ridges, and 200 km for subduction zones.
2. The angle between the strike of the nodal plane and the strike of the plate boundary is smaller than 30°. (3) The tectonic regime of the FMS reflects the plate boundary kinematics, i.e. thrust faulting (TF, TS) near subduction

zones, strike-slip faulting (SS, NS, TS) near oceanic and continental transforms, and normal faulting (NF, NS) near oceanic spreading ridges.

Stress data sets flagged as PBEs are not down-ranked in quality and remain as C-quality in the WSM database. By default they are not plotted on stress maps created with CASMO. For each data set additional information is available in the database which helps the user to evaluate the influence of plate boundary kinematics on the stress orientation at a specific location (distance from and type of the plate boundary). To allow the user to define their own selection criteria for FMS data records we substantially extended in the stress map interface CASMO the filter options for this data type. Further details are given in Heidbach et al. [2010].

2.5 References

Heidbach, O., M. Tingay, A. Barth, J. Reinecker, D. Kurfeß, and B. Müller (2010), Global crustal stress pattern based on the World Stress Map database release 2008, Tectonophys., 482, 3-15, doi:10.1016/j.tecto.2009.07.023.

McKenzie, D. (1969), The relation between fault plane solutions for earthquakes and the directions of the principal stresses, Bull. Seism. Soc. Am., 59(2), 591-601.

Provost, A.-S., J. Chéry, and R. Hassani (2003), 3D mechanical modeling of the GPS velocity field along the North Anatolian fault, Earth Planet. Sci. Lett., 209, 361-377 doi:310.1016/S0012-1821X(1003)00099-00092.

Sperner, B., B. Müller, O. Heidbach, D. Delvaux, J. Reinecker, and K. Fuchs (2003), Tectonic stress in the Earth's crust: advances in the World Stress Map project, in New insights in structural interpretation and modelling, edited by D. A. Nieuwland, pp. 101-116, Geological Society, London.

Zoback, M., and M. L. Zoback (1991), Tectonic stress field of North America and relative plate motions, in Neotectonics of North America, edited by D. B. Slemmons, E. R. Engdahl, M. D. Zoback and D. D. Blackwell, pp. 339-366, Geological Society of America, Boulder, Colorado.

Zoback, M. L. (1992), First and second order patterns of stress in the lithosphere: The World Stress Map Project, J. Geophys. Res., 97, 11703-11728.

Zoback, M. L., and M. Zoback (1980), State of Stress in the Conterminous United States, J. Geophys. Res., 85(B11), 6113-6156.

Zoback, M. L., and M. Zoback (1989), Tectonic stress field of the conterminous United States, in Geophysical Framework of the Continental United States, edited by L. C. Pakiser and W. D. Mooney, pp. 523-539, Geol. Soc. Am. Mem., Boulder, Colorado.

3 Guidelines for the analysis of earthquake focal mechanism solutions

Andreas Barth, John Reinecker and Oliver Heidbach

3.1 Introduction

One of the most evident effects of stress release in the crust are tectonic earthquakes. Due to the large amount of existing earthquake focal mechanisms from regional studies and the steadily increasing number of CMT solutions made routinely public by e.g. the Global CMT Project (formerly by the Harvard seismology group) or the NEIC/USGS, single earthquake focal mechanisms (FMS) make up the majority of data records in the WSM database. Focal mechanism data provide information on the relative magnitudes of the principal stresses, so that a tectonic regime can be assigned.

The determination of principal stress orientations and relative magnitudes from these mechanisms must be done with appreciable caution. Three types of data records from focal mechanisms are distinguished in the WSM database: Single (FMS), formal inversions (FMF), and average/composite (FMA) focal mechanisms. The main difference between these in terms of stress indication is their reliability to indicate regional tectonic stress.

3.2 Single focal mechanisms (FMS)

3.2.1 Determination of FMS

Several methods for determining FMS are in use such as first motion of P waves, polarizations and amplitudes of S waves (e.g. Khattri, 1973), the analysis of P/S amplitude ratios (e.g. Kisslinger et al., 1981) and moment tensor inversion (e.g., Stein and Wysession, 2003). All these methods are using the radiation pattern of seismic rays that expresses the orientation of the active fault and the slip direction (Fig. 3.2-1). These patterns can be used to describe the kinematic processes in the seismic source. Here we focus on the most frequently used methods:

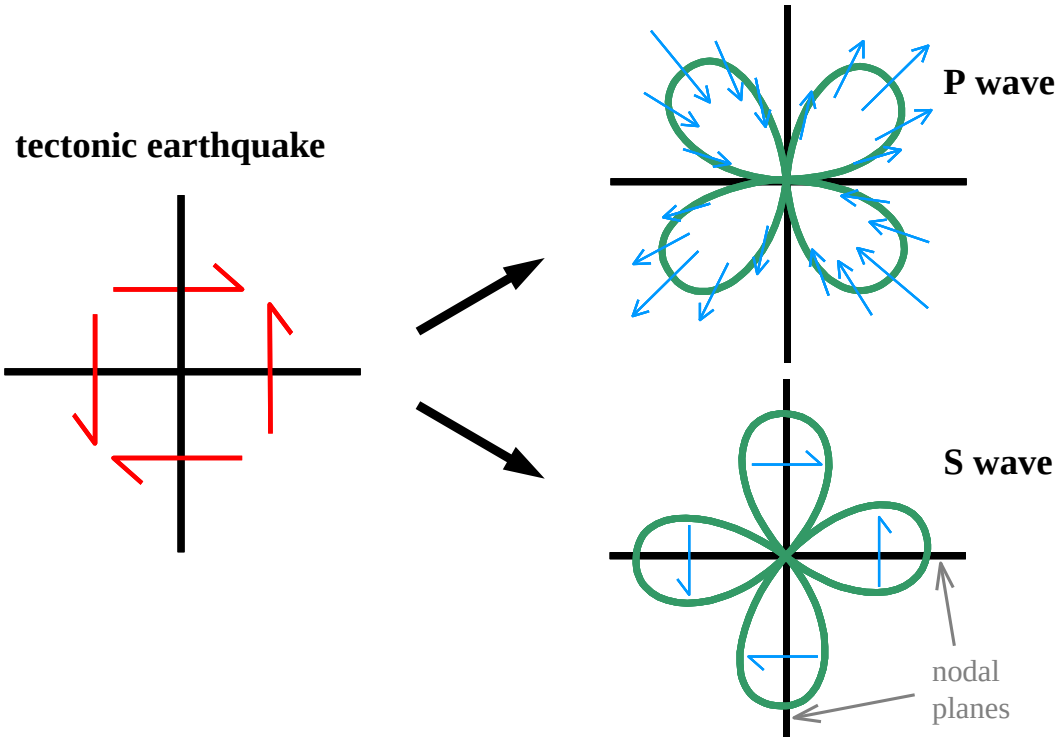

Fig. 3.2-1: P and S wave radiation patterns of a double couple source.

3.2.2 First-motion of P-waves

P-waves radiate relative to the focus with compressional or dilatational initial motion (Fig. 3.2-1). The signal changes in direction of the fault plane and the orthogonal auxiliary plane (both are called nodal planes). Along these planes there is no radiation of P-waves. The first onset of the P-wave on a seismogram of the vertical seismometer component is used to distinguish between a compressional and dilatational first motion of the wave front. The observed first motion is then projected backwards along the ray path onto a conceptual homogeneous unit sphere around the focus (focal sphere), which is thought to be a point source at the very beginning of the rupture event. Any P-wave ray path leaving the source can be identified by two parameters: the azimuth from the source, ϕ, and the angle of emergence, i_0 (Fig. 3.2-2). The angle of emergence is a function of the distance, Δ, between the source and the recording station, and for near stations the crustal model in use. The geographic position of the seismometer is transferred on the focal sphere to a point where the tangent to the ray at the source intersects the focal sphere.

When all available data are plotted in the lower hemisphere of a stereographic projection, two orthogonal nodal planes separating compressional from dilatational first motion can be drawn. The axes of maximum shortening and maximum lengthening bisecting the quadrants are known as the P and the T axes, respectively. Thus, the axes are the principal strain axes that must not necessarily coincide with the principal stress axes.

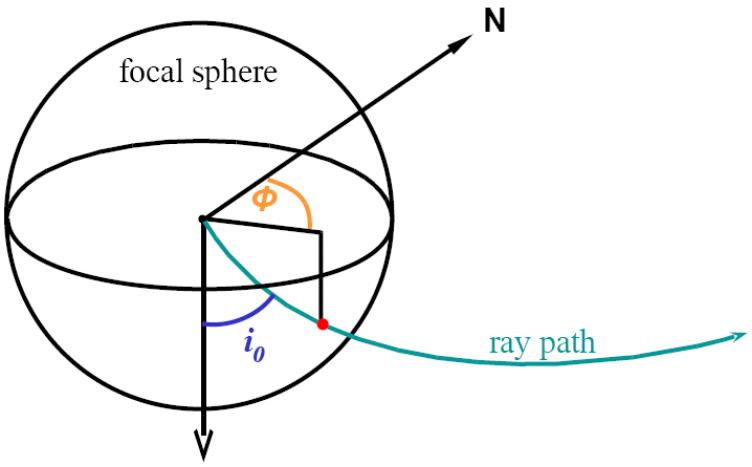

Fig. 3.2-2: Focal sphere of an earthquake source.
Shown is a ray path with azimuth ϕ and angle of emergence i_0.

The P axis lies within the quadrant of dilatational initial motions, whereas the T axis lies within the quadrant of compressional initial motions (Fig. 3.2-3). Both are perpendicular to the intersection of the two nodal planes. The axis formed by this intersection is called the B- or the null axis. The FMS is fully described by the orientation (dip direction and dip) of the P-, T-, and B-axes.

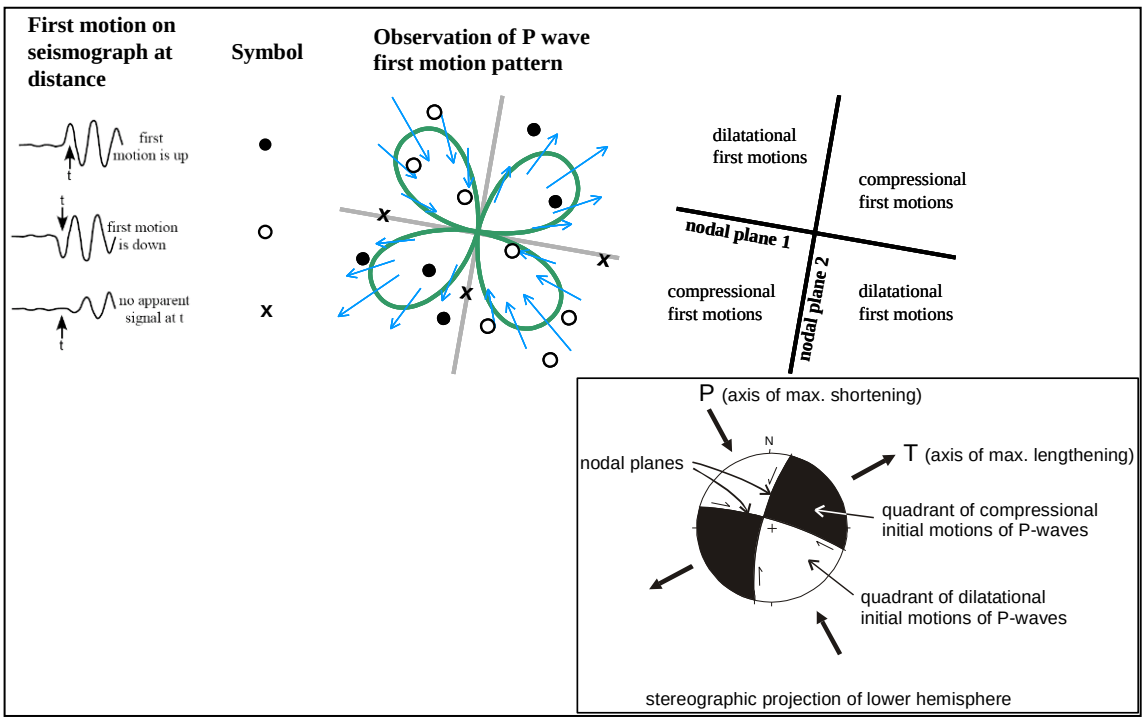

Fig. 3.2-3: Elements of a fault plane solution.

3.2.3 Moment tensor inversion

Moment tensor inversion as well uses the radiation pattern of body- and/or surface-waves. However, here the complete waveform data is inverted to fit synthetic waveforms calculated for a reference earth model (e.g. Jost and Hermann, 1989). The seismic moment tensor ***M*** is a symmetric second order tensor, that describes a variety of seismic sources and consists of the nine couples of equivalent body forces (Fig. 3.2-4).

The off-diagonal elements are assigned to opposite forces that are offset in direction normal to their orientation and thus apply a net torque. However, because of the symmetry of the moment tensor, the conservation of angular momentum is guaranteed. The diagonal elements correspond to force dipoles acting along the coordinate axes. If the earth's structure is known and waveform data is available, the seismic moment tensor ***M*** and thus the focal mechanism of an earthquake can be calculated by inversion. More detailed introductions on moment tensors can be found in Jost and Hermann (1989) or Stein and Wysession (2003) and various textbooks on seismology. Centroid moment tensors (CMT) include the additional inversion for source time and location (Dziewonski et al., 1981) and are routinely provided by the global seismological network GEOFON (http://geofon.gfz-potsdam.de) of the GFZ German Research Centre for Geosciences (http://www.gfz-potsdam.de/) and the Global CMT Project (http://www.globalcmt.org).

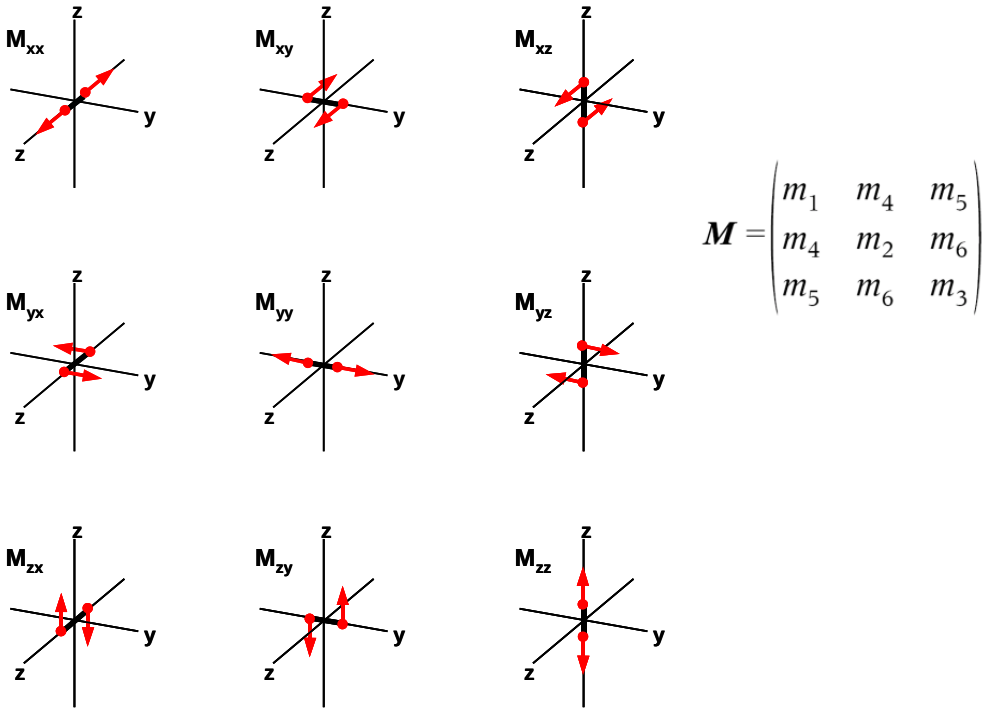

Fig. 3.2-4: The nine force couples of the seismic moment tensor.

3.2.4 Reliability of fault plane solutions

The quality of either solution, determined by moment tensor inversion or first-motion analysis, depends on the knowledge of the earth structure, since both, the source process and the ray path, determine the waveform data. Thus, an insufficient earth model may lead to mapping unexplainable wave parts into the source, resulting in an erroneous focal mechanism. In general, the quality of the solution depends on the number and the quality of the raw data (polarity readings, signal-to-noise ratio, site-effects) and the geographical distribution of the data points relative to the source. Additionally, methodological limitations are due to different fitting algorithm/error-minimisation procedures and the choice of inversion parameters. Regarding moment tensor inversion, the used frequency-band determines the accuracy of the earth model necessary for a reliable inversion (Barth et al., 2007). While low-frequency recordings (long wavelengths) show effects of large-scale earth structures only, high-frequency waveforms (short wavelengths) are influenced by local heterogeneities. This all has to be taken into account for estimating the reliability of a fault plane solution.

3.2.4 Limits of the derivation of stress from FMS

General

The principle axes of the derived moment tensor (P, B, and T) fully describe the focal mechanism and are reported in the WSM database with their azimuth (= dip direction) and plunge (= dip) (in the columns S1AZ, S1PL, S2AZ, S2PL, S3AZ, S3PL). Be aware, that the moment tensor axes of earthquake focal mechanisms are **not** equal to the stress axes! To be strict, the only restriction one can make is that the maximum principal stress (S1) lies within the dilatational quadrant of the focal mechanism (McKenzie, 1969). However, since higher deviations between the P-, B- and T-axes and the principal stress axes S1, S2, and S3 are unlikely they are used as a proxy for the orientation of the stress axes. To account for this inaccuracy, data derived from single focal mechanism (FMS) are given a quality of not better than C regardless of the size of the earthquake and how well the focal mechanism is constraint (see Chapter 6). The limits of stress derivation from FMS are limited by the fault-plane ambiguity and the coefficient of friction:

Fault plane ambiguity

Because of the symmetry of the force double couple and moment tensor on which it is based, the FMS beachball diagram has a crystal-like regularity to it:

1. The two nodal planes are perpendicular to each other.
2. The pole of the auxiliary plane is colinear with the slip vector on the fault plane.
3. The B-axis is coincident with the intersection of the two nodal planes, and so is contained within both of the nodal planes.

4. The P-axis is in the middle of the quadrant with dilatational (down) first motions, and the T-axis is in the middle of the quadrant with compressional (up) first motions.
5. The T- and P-axes bisect the dihedral angles between the nodal planes; that is, the T- and P-axes are 45° from the nodal planes.
6. The P-, T- and B-axes are orthogonal to one another.
7. The plane defined by the T- and P-axes also contains the vectors normal to the nodal planes, one of which is the slip vector.

Therefore, on the basis of polarity readings or moment tensor inversion alone, it cannot be decided which nodal plane is the fault plane. This can only be decided by calculating higher degree moment tensors (Dahm and Krüger, 1999), the analysis of aftershock distributions (commonly located on the rupture plane), field evidence from surface rupture in case of strong earthquakes, or seismotectonic considerations. Taking into account additional data on azimuthal amplitude and frequency or wave-form patterns, which are controlled by the Doppler effect of the moving source may allow resolving this ambiguity too. The latter can be studied more easily in low-frequency teleseismic recordings while in the local distance range high-frequency waveforms and amplitudes may be strongly influenced by resonance effects due to low-velocity near-surface layers.

3.2.5 Internal friction, stress orientations and possible plate boundary events

One should also be aware that the assumed angle of 45° between the fault plane and S1 and S3 is only true in case of new fracture generation in a homogeneous isotropic medium. In this case the principal axes of the seismic moment tensor (the principal strain axes) would coincide with the principal stress axes. However, this may not be correct in a heterogeneous anisotropic medium (as the crust), a given stress environment and tectonic situation. In by far most cases tectonic earthquakes represent reactivation of faults in shear. Because of the fault plane ambiguity it is not known a priori which of the two nodal planes of the focal mechanism is the rupture plane and the P-, B- and T-axes are used as a proxy for the orientation of the principal stress axes.

Townend (2006) reviews the difference between P-, B-, T- and S1-, S2-, S3-axes for plate boundary strike-slip faults and shows that these faults are oriented at higher angles to the orientation of maximum horizontal compressive stress S_H than a typical internal friction assumed for the brittle continental crust would suggest. Since earthquakes concentrate on plate boundaries the influence of plate boundary geometry might be dominating the overall kinematics and therefore the inferred "stress" orientations. Plate boundaries are characterized by faults with preferred orientations and presumably include major faults with a low coefficient of internal friction. These faults can not sustain high shear stresses, and thus can be reactivated even when S_H is almost perpendicular to the fault strike (e.g. Zoback et al, 1987). Thus, the orientation of the P-, B-, and T-axis from FMS could deviate

considerably from the principal stress orientations. To account for this inaccuracy data derived from FMS are given a quality of not better than C regardless of the size of the earthquake and how well the focal mechanism is constraint. Assuming that major plate boundaries are weak in general, FMS data records in their vicinity are flagged as Possible Plate Boundary Events (PBE) when three criteria are valid:

1. The event is located within a critical distance d_{crit} relative to the closest plate boundary segment. This critical distance depends on the plate boundary type following the global plate boundary type classification of Bird (2003). We estimated d_{crit} by means of a statistical analysis as being 45 km for continental transform faults, 80 km for oceanic transform faults, 70 km for oceanic spreading ridges, and 200 km for subduction zones.
2. The angle between the strike of the nodal plane and the strike of the plate boundary is smaller than 30°.
3. The tectonic regime of the FMS reflects the plate boundary kinematics, i.e. thrust faulting (TF, TS) near subduction zones, strike-slip faulting (SS, NS, TS) near oceanic and continental transforms, and normal faulting (NF, NS) near oceanic spreading ridges.

Stress data records flagged as PBE are not down-ranked in quality and remain as C-quality in the WSM database. By default they are not plotted on stress maps created with CASMO (online database interface; http://www.world-stress-map.org/casmo). For each data record additional information (plate boundary type and distance) is available in the database, which helps the user to evaluate the influence of plate boundary kinematics on the stress orientation at a specific location.

3.3 Formal stress inversions of focal mechanisms (FMF)

A better estimation of the tectonic stress orientation can be achieved when a set of FMS is available for a region with a homogeneous regional stress field. These FMS can be combined to determine the orientations of the principle stress axes by a formal inversion. The formal stress inversion of several FMS improves the quality of stress derivation, but is linked to two main assumptions: (1) It is assumed that the chosen FMS lie in a region with a uniform stress field that is invariant in space and time. The binning technique can be either hypothesis-driven to prove e.g. stress rotations or be data-driven. Hardebeck and Michael (2004) give a detailed discussion on the differences between the binning techniques. To overcome the subjectivity of manual binning Townend and Zoback (2006) used an non-hierarchical clustering algorithm to group FMS in Japan for stress inversion. (2) It is assumed, that the direction of earthquake slip occur in direction of maximum shear stress (Wallace-Bott hypothesis, Bott, 1959).

A stress inversion determines the orientation of the principal stresses that minimises the average difference between the slip vector and the orientation of maximum shear stress on the inverted faults. This angle is commonly called “misfit angle”. Different algorithms of stress inversion have been developed by various authors (the most common routines are

described by Gephart and Forsyth, 1984; Michael, 1984; Angelier, 1979; Rivera and Cisternas, 1990). A major difference between stress inversion techniques is the handling of the fault plane ambiguity. Since stress inversion was first used for slickenside field data, some algorithms need the fault plane to be determined a priori. In most cases this is not possible, since further information is to determine the fault plane. Angelier (2002) provided a method automatically choosing the fault plane. Gephart and Forsyth (1984) perform the inversion as if all nodal planes were independent data, primary and remove the worse fitted auxiliary planes in a second step. The final inversion then includes the planes that are best fitted by a uniform stress field. A third approach applies a bootstrap routine that picks *x* mechanisms at random from the original *x* events. Each dataset than will have some mechanisms repeated two or more times (Michael, 1987). Random decisions of the true fault plane and a variety of bootstrapped datasets finally give a statistical determination of the stress orientation. A recent approach additionally includes a-priori information on the stress field into a probabilistic stress analysis of FMS that accounts for the fault plane ambiguity by calculating probability density functions for the orientations of the principal stress axes (Arnold and Townend, 2007). The different inversion techniques all result in a deviatoric stress tensor, which gives four parameters, the orientation of the three principal stress axes and the relative magnitudes of the intermediate principal stress with respect to the maximum and minimum principal stress. However, stress inversion is not capable of determining stress magnitudes.

The three principal stress axes (reported in the WSM database columns S1AZ, S1PL, S2AZ, S2PL, S3AZ, S3PL) plus the stress ratio of the stress magnitudes RATIO=(S1-S2)/(S2-S3) build up the reduced stress tensor. For the incorporation of new FMF data the specification of RATIO is mandatory. The availability of this information enables to calculate the shape and orientation of the stress ellipsoid and thus the true orientation of S_H. It is recommended to use the formulas given by Lund and Townend (2007) for S_H-determination when the reduced (or full) stress tensor is available.

The adequate binning into regions with a constant stress field in space and time is crucial, but still under debate, especially for regions near to major plate boundaries. Here, dominating fault orientations may distort the inferred stress orientations, what may also count for some intraplate regions. It is still in question, whether plate boundary faults are fundamentally different from smaller intraplate faults. For the discussion of these aspects we refer to the studies of Townend and Zoback (2006) and Hardebeck and Michael (2004).

3.4 Average or composite focal mechanisms (FMA)

In contrary to a stress inversion, averaging the data or the construction of composite solutions does not take into account the conceptional difference between the stress tensor and the moment tensor (see Chapter 2.2.) and therefore this technique is getting out of use.

3.4.1 Average focal mechanisms

Despite the fact that the P-axis of a focal mechanism does not necessarily correlate with the orientation of S1, regional compilations show that the average orientation for P-, B-, and T-axes determined from a number of earthquakes gives a good indication of the maximum compressive stress orientation throughout a region (Sbar and Sykes, 1973, Zoback and Zoback, 1980). Because of the circular distribution of P-, B-, and T-axes, they need careful treatment when being averaged, and ignoring the plunge when averaging trends is also problematic (Lund and Townend, 2007).

Anyhow, there are no advantages of an average mechanism compared to FMF since the matter of an adequate binning is relevant for both methods. In future, FMF should be preferred to FMA, since FMF considers the difference between stress tensor and moment tensor, where FMA does not.

3.4.2 Composite focal mechanisms

When the main shock of an earthquake is only detected within a limited region and the amount and azimuthal distribution of first motions is not sufficient to construct a focal mechanism from this single event, composite focal mechanisms are constructed by superimposing data from aftershocks or other events rupturing the same fault segment (Sbar et al., 1972). For this one major assumption is that all aftershocks used have the same focal mechanism, i.e. have the same radiation pattern, as the main shock. This is reasonable if aftershocks occur along the same fault as the main shock. However, in practice, aftershocks do not necessarily occur along the same fault plane responsible for the main shock. Some aftershocks may occur on faults of a much different orientation from the main shock. Hence, composites rarely show a perfect separation of compressional and dilatational first motions. Aftershocks are often recorded by portable seismic networks from near distance. Superposition requires locating each aftershock in order to calculate ϕ and i_0 for each portable recording station. A composite plot of ray paths cutting the focal sphere is made by moving the centre of the stereonet to the hypocentre of each aftershock. Because of the close recording distance to the aftershock, an upper hemisphere projection of ϕ and i_0 is more convenient. Calculation of the appropriate angle of emergence becomes more critical for larger and deeper earthquakes in areas with a more complex crustal structure.

3.5 Tectonic stress regime

As the focal mechanism gives information on the faulting type (normal faulting, NF; strike-slip SS; thrust faulting TF), the relative magnitudes of S_H, S_h and S_V are known. Besides the NF, TF, and SS categories, combinations of NF with SS (transtension NS) and TF with SS (transpression TS) exist (Zoback, 1992). NS is appropriate where the maximum stress or P-

axis is the steeper plunging of the P- and B-axis. TS is a appropriate where the minimum stress or T-axis is the steeper plunging of the B- and T-axis. The plunges (pl) of P-, B-, and T-axis (or σ_1, σ_2, and σ_3 axis for FMF data records) are used to assign the appropriate stress regime to the data record (see Tab. 3.5-1 and Fig. 3.5-1).

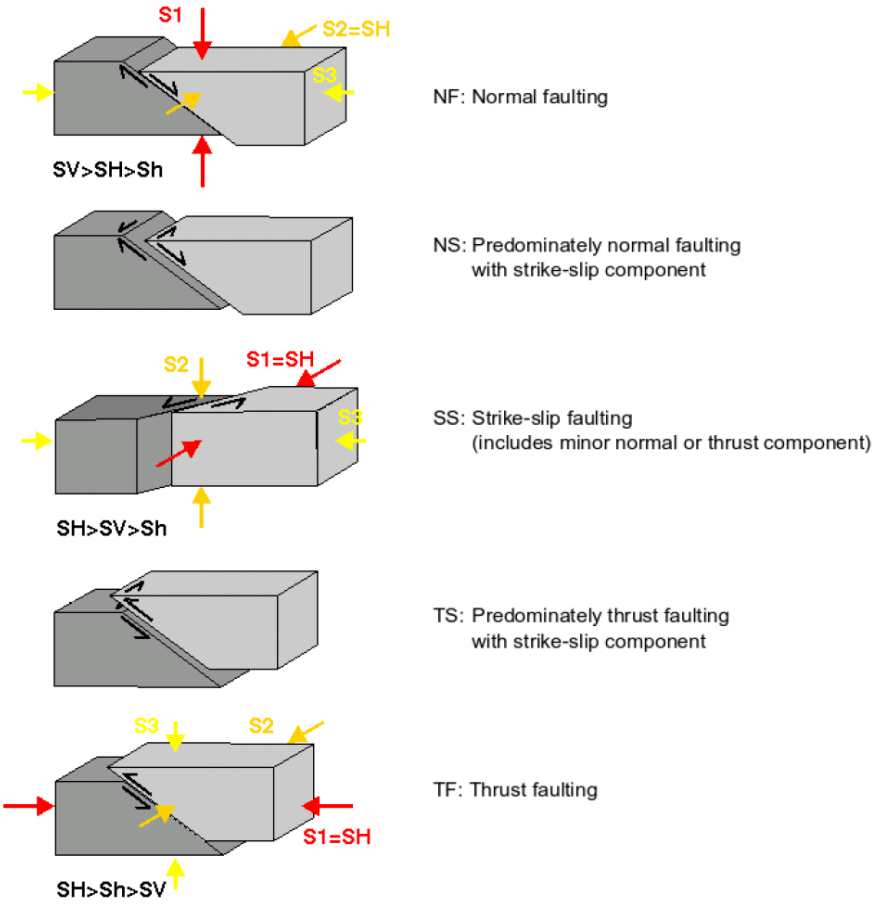

Fig. 3.5-1 Tectonic stress regime classification.

Schematic illustration of the five general tectonic regimes and the according orientations of the principle stress axes (after Anderson, 1951, and Zoback, 1992).

Tab. 3.5-1: Tectonic regime assignment.

The numbers in the table are subjective choices and taken from Zoback (1992)

P/S1-axis	B/S2-axis	T/S3-axis	Regime	S_H-azimuth
pl > 52		pl < 35	NF	azim. of B-axis
40 < pl < 52		pl < 20	NS	azim. of T-axis + 90°
pl < 40	pl > 45	pl < 20	SS	azim. of T-axis + 90°
pl < 20	pl > 45	pl < 40	SS	azim. of P-axis
pl < 20		40 < pl < 52	TS	azim. of P-axis
pl < 35		pl > 52	TF	azim. of P-axis

The exact cut-off values defining the tectonic regime categories are subjective. Zoback (1992) used the broadest possible categorization consistent with actual P-, B-, and T-axes values. The choice of axes used to infer the S_H orientation is displayed in the table above, e.g. the S_H orientation is taken as the azimuth of the B-axis in case of a pure normal faulting regime (NF) and as 90° + T-axis azimuth in the NS case when the B-axis generally plunges more steeply than the T-axis. The data which fall outside these categories are assigned to an unknown stress regime ("U") and are given an E-quality indicating that the maximum horizontal stress orientation is not defined.

3.6 WSM quality criteria for FMS, FMF and FMA data

All data in the WSM database are quality ranked to facilitate comparison between different indicators of stress orientation (e.g. focal mechanism solutions, drilling-induced tensile fractures, overcoring). The quality ranking criteria for stress orientations determined from focal mechanisms are presented in Tab. 3.6-1, 3.6-2, and 3.6-3.

Ideally, the regional stress field would be estimated from a number of events in a given area with a broad azimuthal distribution of fault orientations. The more reliable stress orientation is reflected in the higher WSM quality for the formal inversion of several focal mechanisms (FMF). A-quality data are believed to record the stress orientation to within ±15°, B-quality data to within ± 20°. Single focal mechanisms (FMS) are given a C-quality indicating their reliability to within ± 25°.

Composite as well as average focal mechanisms (FMA) do not take into account the conceptional difference between the stress tensor and the moment tensor. So they might be even less precise in fault plane orientations than FMS and are assigned to D-quality (reliable within ± 40°).

Criteria for down-ranking the WSM quality are:

- a low number of used seismic stations
- large gaps in the azimuthal coverage
- instability of the solution due to minor changes in the dataset or in the inversion parameters
- a high CLVD and/or isotropic part in the moment tensor (Jost and Hermann, 1989)
- a high mathematical standard deviation and data variance

Tab. 3.6-1: WSM quality criteria for FMF data.

World Stress Map quality ranking criteria for data records from formal stress inversion of single focal mechanisms (s.d. = standard deviaion)

A-Quality	B-Quality	C-Quality	D-Quality	E-Quality
Formal inversion of ≥ 15 well constrained single event solutions in close geographic proximity and s.d. or misfit angle ≤ 12°	Formal inversion of ≥ 8 well constrained single event solutions in close geographic proximity and s.d. or misfit angle ≤ 20°	-	-	-

Tab. 3.6-2: WSM quality criteria for FMS data.

World Stress Map quality ranking criteria for single focal mechanisms FMS (M = local magnitude)

A-Quality	B-Quality	C-Quality	D-Quality	E-Quality
-	-	• Well constraint single event solution ($M \geq 2.5$) • (e.g. CMT solutions)	• Well constrained single event solution ($M < 2.5$)	• Mechanism with P,B,T axes all plunging 25°-40° • Mechanism with P and T axes both plunging 40°-50°

Tab. 3.6-3: WSM quality criteria for FMA data.

World Stress Map quality ranking criteria for average and composite focal mechanisms.

A-Quality	B-Quality	C-Quality	D-Quality	E-Quality
-	-	-	• Average of P-axis • Composite solutions	• Mechanism with P,B,T axes all plunging 25°-40° • Mechanism with P and T axes both plunging 40°-50°

3.7 References

Anderson, E.M., 1951. The dynamics of faulting and dyke formation with application to Britain, 2nd ed., Edinburgh, Oliver and Boyd.

Angelier, J., 1979. Determination of the mean principal directions of stresses for a given fault population, Tectonophysics, 56, T17-T26.

Angelier, J., 2002. Inversion of earthquake focal mechanisms to obtain the seismotectonic stress IV - a new method free of choice among the nodal planes, Geophys. J. Int., 150, 588-609.

Arnold, R. and Townend, J., 2007. A Bayesian approach to estimating tectonic stress from seismological data. Geophys. J. Int., 170, 1336-1356.

Barth, A., Wenzel, F. and Giardini, D., 2007. Frequency sensitive moment tensor inversion for light to moderate magnitude earthquakes in eastern Africa. Geophys. Res. Lett., 34, L15302.

Bird, P., 2003. An updated digital model for plate boundaries. Geochem. Geophys. Geosyst., 4(3): 1027, doi:10.1029/2001GC000252.

Bott, M.H.P., 1959. The mechanics of oblique slip faulting. Geol. Mag., 96, 109-117.

Byerlee, J.D., 1978. Friction of rocks. Pure Appl. Geophys., 116: 615-626.

Dahm, T. and Krüger, F., 1999. Higher-degree moment tensor inversion using far-field broad-band recordings: theory and evaluation of the method with application to the 1994 Bolivia deep earthquake. Geophys. J. Int., 137, 35-50.

Dziewonski, A.M., Chou, T.-A. and Woodhouse, J.H., 1981. Determination of earthquake source parameters from waveform data for studies of global and regional seismicity. J. Geophys. Res., 86: 2825-2852.

Gephart, J.W. and Forsyth, D.W., 1984. An Improved Method for Determining the Regional Stress Tensor Using Earthquake Focal Mechanism Data: Application to the San Fernando Earthquake Sequence, J. Geophys. Res., 89, 9305-9320.

Hardebeck, J.L., Michael, A., 2004. Stress orientations at intermediate angels to the San Andreas Fault, California. J. Geophys. Res., 109(B11303): doi:10.1029/2004JB003239.

Jost, M.L. and Hermann, R. B., 1989. A Student's Guide to and Review of Moment Tensors, Seism. Res. Lett., 60, 37-57.

Khattri, K., 1973. Earthquake focal mechanism studies─A review, Earth Sci. Rev., 9, 19-63.

Kisslinger, C., Bowman, J.R., and Koch, K., 1981. Procedures for computing focal mechanisms from local (SV/P) data, Bull. Seism. Soc. Am., 71, 1719–1729.

Lund, B. and Townend, J., 2007. Calculating horizontal stress orientations with full or partial knowledge of the tectonic stress tensor. Geophysical Journal International, 170, 1328-1335.

McKenzie, D.P., 1969. The relation between fault plane solutions for earthquakes and the directions of the principal stress. Bull. Seism. Soc. Am., 59, 591-601.

Michael, A.J., 1984. Determination of stress from slip data: Faults and folds, J. Geophys. Res., 89, 11,517-11,526.

Michael, A.J., 1987. Use of Focal Mechanisms to Determine Stress: A Control Study, J. Geophys. Res., 92, 357-368.

Rivera, L. and Cisternas, A., 1990. Stress tensor and fault plane solutions for a population of earthquakes . Bull. Seism. Soc. Am., 80, 600-614.

Sbar, M.L., Barazangi, M., Dorman, J., Scholz, C.H., Smith, R.B., 1972. Tectonics of the Intermountain Seismic Belt, western United States, Microearthquake seismicity and composite fault plane solutions. Geological Society of America Bulletin, 83: 13-28.

Sbar, M.L., Sykes, L.R., 1973. Contemporary compressive stress and seismicity in eastern North America, An example of intraplate tectonics. Geol. Soc. Am. Bull., 84: 1861-1882.

Stein, S. and Wysession, M., 2003. An introduction to seismology, earthquakes, and earth structure, Blackwell Publishing.

Townend, J. 2006. What do Faults Feel? Observational Constraints on the Stresses Acting on Seismogenic Faults, Earthquakes: Radiated Energy and the Physics of Faulting, Geophysical Monograph Series 170, 313-327.

Townend, J. and Zoback, M.D., 2006. Stress, strain, and mountain building in central Japan. J. Geophys. Res., 111, B03411.

Wallace, R.E., 1951. Geometry of shearing stress and relation to faulting. J. Geol., 59: 118-130.

Zoback, M.L., 1992. First- and second-order patterns of stress in the lithosphere: The World Stress Map project. J. Geophys. Res., 97, 11,703-11,728.

Zoback, M.L., Zoback, M.D., 1980. Faulting patterns in north-central Nevada and strength of the crust. Journal of Geophysical Research, 85: 275-284.

Zoback, M.D., Zoback, M.L., Mount, V.S., Suppe, J., Eaton, J.P., Healy, J.H., Oppenheimer, D.H., Reasenberg, P.A., Jones, L., Raleigh, C.B., I.G., W., Scotti, O., Wentworth, C., 1987. New Evidence of the State of Stress of the San Andreas Fault System. Science, 238: 1105-1111.

4 Guidelines for borehole breakout analysis from four-arm caliper logs

John Reinecker, Mark Tingay and Birgit Müller

4.1 Introduction

Borehole breakouts are an important indicator of horizontal stress orientation, particularly in aseismic regions and at intermediate depths (< 5 km). Approximately 19% of the stress orientation indicators in the WSM database have been determined from borehole breakouts. Here we present the procedures for interpreting borehole breakouts from four-arm caliper log data and for WSM quality ranking of stress orientations deduced from borehole breakouts.

4.2 Borehole Breakouts

Borehole breakouts are stress-induced enlargements of the wellbore cross-section (Bell and Gough, 1979). When a borehole is drilled the material removed from the subsurface is no longer supporting the surrounding rock. As a result, the stresses become concentrated in the surrounding rock (i.e. the wellbore wall). Borehole breakout occurs when the stresses around the borehole exceed that required to cause compressive failure of the borehole wall (Zoback et al., 1985; Bell, 1990). The enlargement of the wellbore is caused by the development of intersecting conjugate shear planes, that cause pieces of the borehole wall to spall off (Fig. 4.2-1).

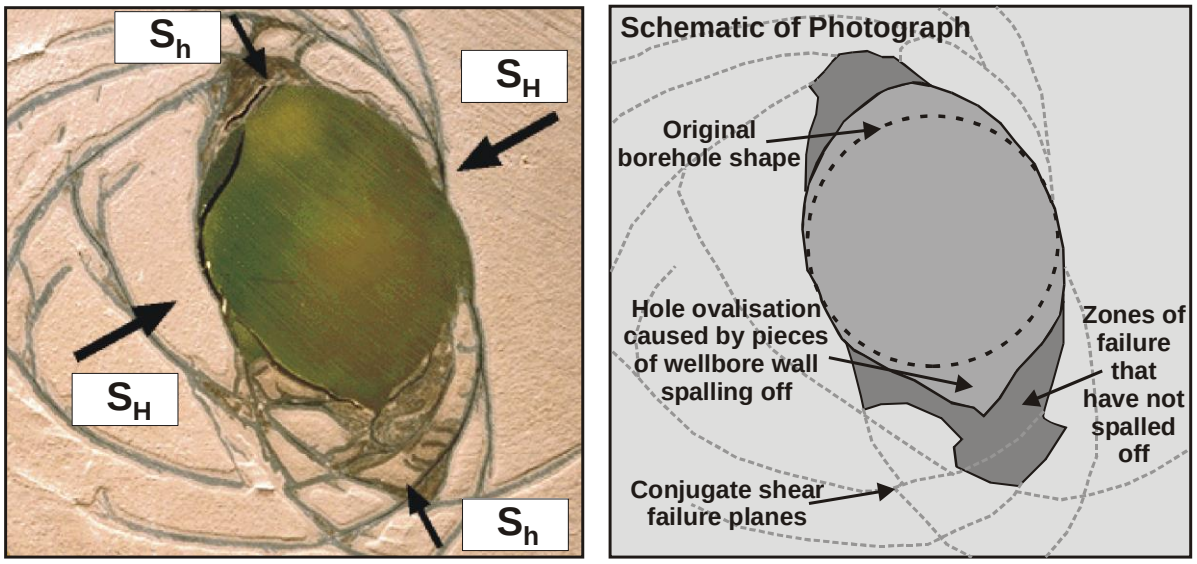

Fig. 4.2-1: Borehole breakout from a lab experiment.

Results of a hollow cylinder lab test simulating borehole breakout (performed by the CSIRO Division of Geomechanics). Intersection of conjugate shear failure planes results in enlargement of the cross-sectional shape of the wellbore. S_{Hmax} and S_{hmin} refer to the orientations of maximum and minimum horizontal stress respectively.

Around a vertical borehole stress concentration is greatest in the direction of the minimum horizontal stress $S_{hmin.}$ Hence, the long axes of borehole breakouts are oriented approximately perpendicular to the maximum horizontal stress orientation S_{Hmax} (Plumb and Hickman, 1985).

4.3 Four-Arm Caliper Tools

Four-arm caliper tools (such as Schlumberger's HDT, SHDT and OBDT) are commonly run in the hydrocarbon industry to obtain information about the formation (primarily strike and dip of bedding) and to estimate the volume of cement required for casing. However, unprocessed oriented four-arm caliper logs can also be used to interpret borehole breakouts. The logs needed for interpretation are (nomenclature given on Fig. 4.3-1):

- Azimuth of pad 1 (P1AZ) relative to magnetic north;
- diameter of the borehole in two orthogonal directions ('Caliper 1' (C1) between pad 1 and 3 and 'Caliper 2' (C2) between pad 2 and 4);
- borehole deviation (DEVI) from vertical;
- azimuth of borehole drift (HAZI), and;
- bearing of pad 1 relative to the high side of the hole (RB).

Depth, C1, C2 and DEVI must be available to interpret breakouts. However, only two of P1AZ, RB and HAZI are necessary as the missing log can be calculated using following equation:

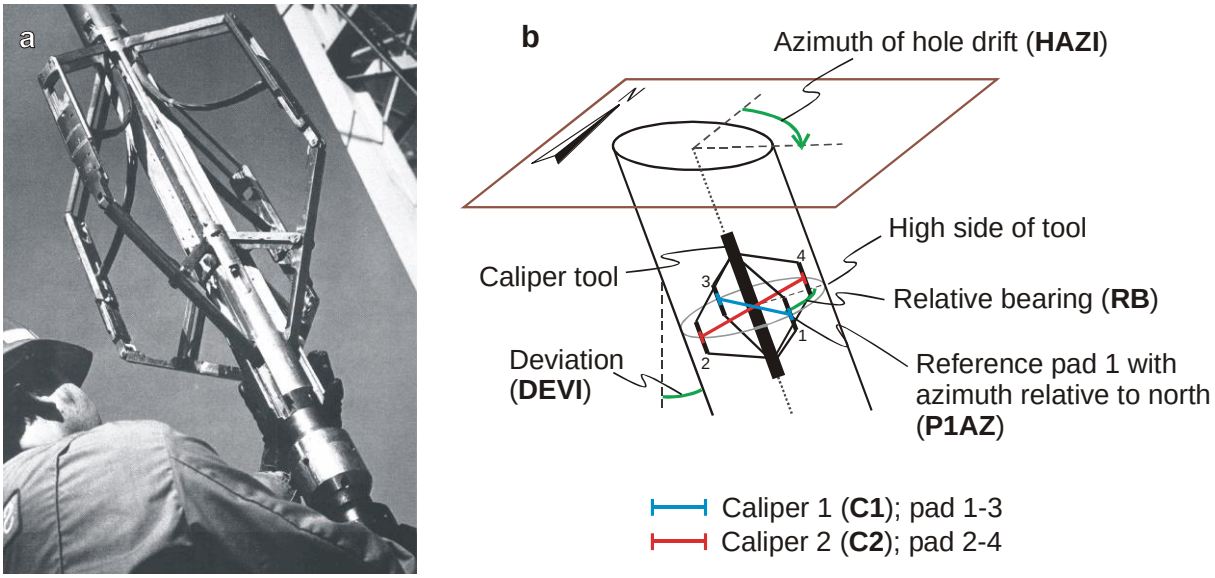

Fig. 4.3-1: Schlumberger High-resolution Dipmeter Tool (HDT).

a) The Schlumberger High-resolution Dipmeter Tool (HDT; from Plumb and Hickman, 1985). Note the four orthogonal caliper arms. b) Geometry of the four-arm caliper tool in the borehole and data used for interpreting borehole breakouts.

4.4 Interpreting Breakouts from Four-Arm Caliper Data

The four-arm caliper tool will rotate as it is pulled up the borehole due to cable torque. However, the tool stops rotating in zones of borehole enlargement if one caliper pair becomes 'stuck' in the enlargement direction (Plumb and Hickman, 1985; Fig. 4.4-1). The combined use of the six logs listed above enables the interpreter to distinguish zones of stress-induced breakouts from other borehole enlargements such as washouts and key seats (Fig. 4.4-1 and Fig. 4.4-2). To identify zones

of breakout and the orientation of the enlargement we suggest the criteria in Table 1 (based on Plumb and Hickman, 1985; Bell, 1990; Zajak and Stock, 1997):

Tab. 4.4-1: Detection criteria borehole breakouts from four-arm caliper data.

1. Tool rotation must cease in the zone of enlargement.
2. There must be clear tool rotation into and out of the enlargement zone.
3. The smaller caliper reading is close to bit size. Top and bottom of the breakout should be well marked.
4. Caliper difference has to exceed bit size by 10 %.
5. The enlargement orientation should not coincide with the high side of the borehole in wells deviated by more than 5°.
6. The length of the enlargement zone must be greater than 1 m.

Breakout orientations can rotate in inclined boreholes and may not always directly yield the horizontal stress orientations (Mastin, 1988; Peska and Zoback, 1995). Hence, the maximum horizontal stress orientation can only be reliably estimated from breakouts in approximately vertical boreholes (less than 10° deviation from the vertical). All orientations measured from four-arm caliper tools need to be corrected for the local magnetic declination at the time of measurement.

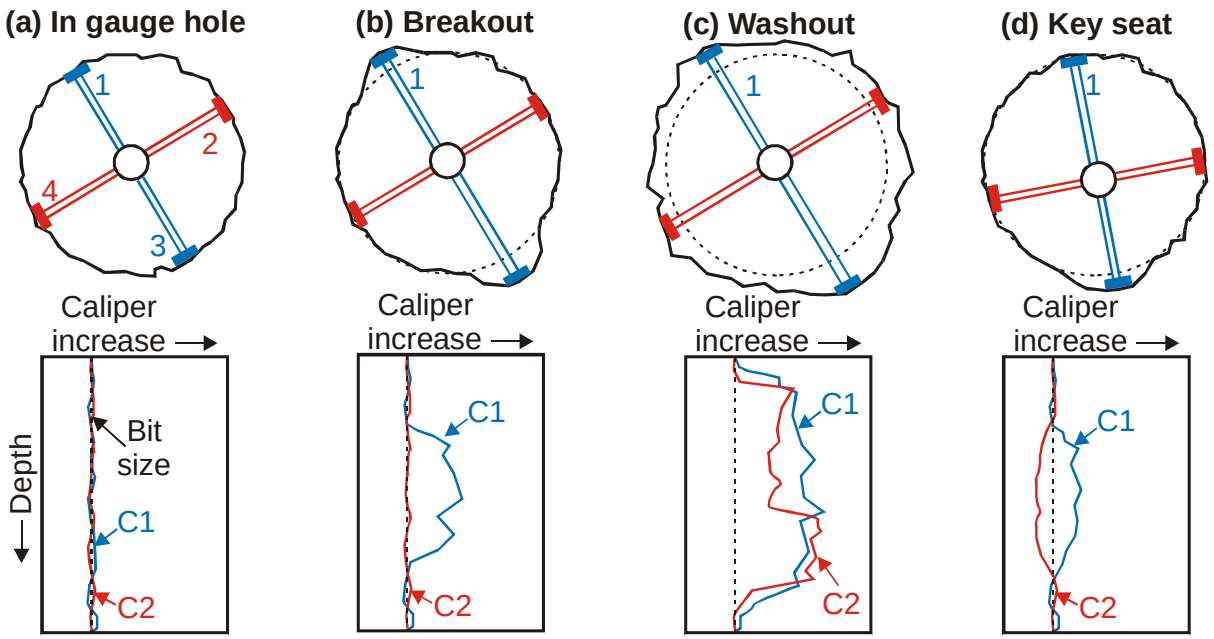

Fig. 4.4-1: Common types of enlarged borehole and their caliper log response.
Figure is modified after Plumb and Hickman (1985).

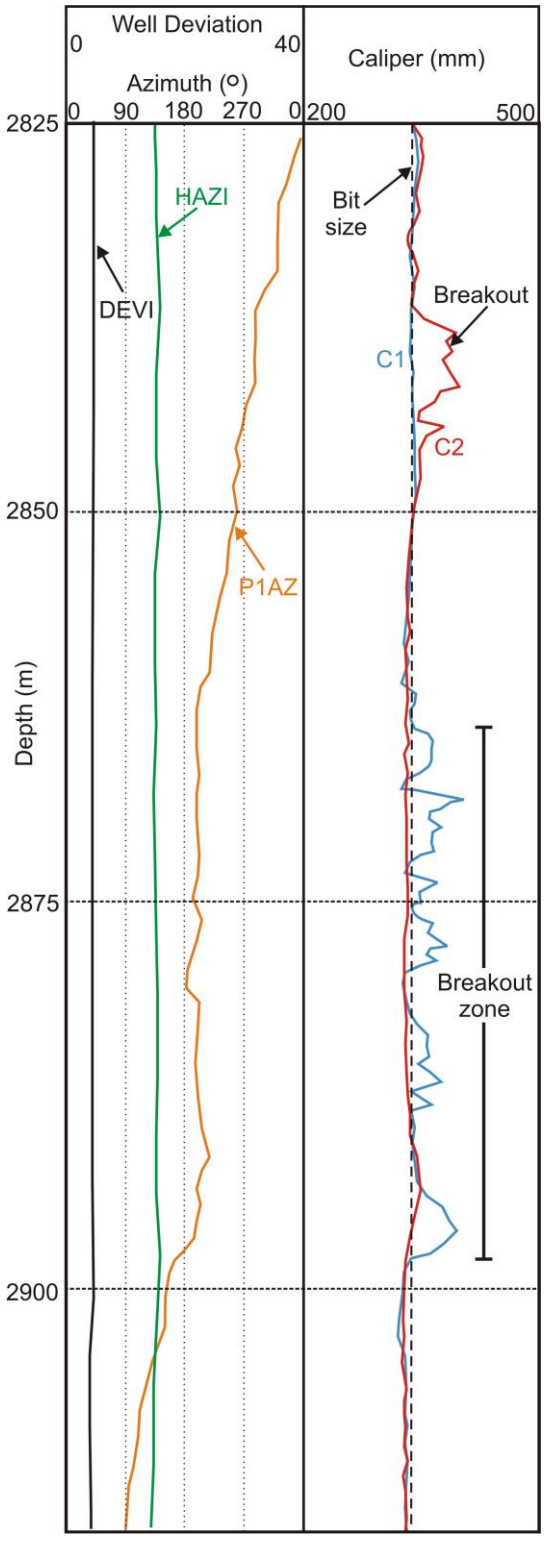

Fig. 4.4-2: Four-arm caliper log example.

Caliper log plot displaying borehole breakouts. Caliper one (C1) locks into breakout zone from 2895-2860 m (P1AZ ≈ 200°), the tool then rotates 90° and Caliper two (C2) locks into another breakout from 2845-2835 m (P1AZ ≈ 290°). Both breakout zones are oriented approximately 020° and suggest a S_{Hmax} direction of 110°. The borehole is deviated 4° (DEVI) towards 140° (HAZI).

4.5 Determining the mean S_{Hmax} orientation with circular statistics

Breakout orientations are bimodal data. Data between 180° and 360° are equivalent to those between 0° and 180° (S_H varies between 0° and 180°). According to Mardia (1972) the mean breakout azimuth θ_m (i.e. S_h) of a population of n picked breakout directions θ_i is derived by first transforming the angles to the 0-360° interval. $\theta_i^* = 2\ \theta_i$

Then, the direction cosine and sine have to be added and averaged either by the number of measurements (for number weighted mean) or by the total breakout length L (length weighted mean).

number weighted:

$$C = \frac{1}{n}\sum_{i=1}^{n} \cos\theta_i^*$$

$$S = \frac{1}{n}\sum_{i=1}^{n} \sin\theta_i^*$$

length weighted:

$$L = \sum_{i=1}^{n} l_i$$

$$C = \frac{1}{L}\sum_{i=1}^{n} l_i \cos\theta_i^*$$

$$S = \frac{1}{L}\sum_{i=1}^{n} l_i \sin\theta_i^*$$

where l_i is the length of breakout i with orientation θ_i^*.

The mean azimuth results from: $\theta_m = ½ \arctan(S/C)$

(Make sure that the angles are converted from rad into deg!)

The standard deviation s_o is derived as

$s_o = 360/2\pi\ (-1/2\ \log_e R)^{1/2}$ with $R = (C^2 + S^2)^{1/2}$.

4.6 WSM quality criteria for BO data from caliper logs

All data in the WSM database are quality ranked to facilitate comparison between different indicators of stress orientation (e.g. focal mechanism solutions, drilling-induced tensile fractures, overcoring). The quality ranking criteria for stress orientations determined from breakouts interpreted from four-arm caliper logs is presented in Tab. 4.6-1.

Tab. 4.6-1: WSM quality criteria for BO data from caliper logs.

World Stress Map quality ranking criteria for borehole breakouts (s.d. = standard deviation).

A-Quality	B-Quality	C-Quality	D-Quality	E-Quality
Wells that have ten or more distinct breakout zones with a combined length > 300 m; and with s.d. ≤ 12°	Wells that have at least six distinct breakout zones with a combined length > 100 m; and with s.d. ≤ 20°	Wells that have at least four distinct breakouts zones with a combined length > 30 m; and with s.d. ≤ 25°	Wells that have less than four breakouts zones or a combined length < 30 m or with s.d. > 25°	Wells with no reliable breakouts detected or with extreme scatter of breakout orientations (s.d. > 40°)

4.7 References

Bell, J.S. (1990): Investigating stress regimes in sedimentary basins using information from oil industry wireline logs and drilling records. - In: Hurst, A., M. Lovell and A. Morton (eds.): Geological applications of wireline logs, Geol. Soc. Lond. Spec. Publ., 48, 305-325.

Bell, J.S. and D.I. Gough (1979): Northeast-southwest compressive stress in Alberta: evidence from oil wells. - Earth Planet. Sci. Lett., 45, 475-482.

Mardia, K.V. (1972): Statistics of directional data: probability and mathematical statistics. - 357 pp., London (Academic Press).

Mastin, L. (1988): Effect of borehole deviation on breakout orientations. - J. Geophys. Res., 93, 9187-9195.

Peska, P. and M. D. Zoback (1995): Compressive and tensile failure of inclined well bores and determination of in situ and rock strength. - J. Geophys. Res., 100, 12791-12811.

Plumb, R.A. and S.H. Hickman (1985): Stress-induced borehole enlargement: a comparison between the four-arm dipmeter and the borehole televiewer in the Auburn geothermal well. - J. Geophys. Res., 90, 5513-5521.

Sperner, B., B. Müller, O. Heidbach, D. Delvaux, J. Reinecker and K. Fuchs (2003): Tectonic Stress in the Earth's Crust: Advances in the World Stress Map Project. - In: Nieuwland D. (ed.): New Insights into Structural Interpretation and Modelling, Geol. Soc. Lond. Spec. Publ., 212, 101-116.

Zajac, B.J. and J.M. Stock (1992): Using Borehole Breakouts to Constrain the Complete Stress Tensor: Results from the Sijan Deep Drilling Project and Offshore Santa Maria Basin California. - J. Geophys. Res., 102, 10083-10100.

Zoback, M.D., D. Moos, L.G. Mastin and R.N. Anderson (1985): Well bore breakouts and in situ stress. - J. Geophys. Res., 90, 5523-5530.

5 Guidelines for borehole breakout and drilling-induced fracture analysis from image logs

Mark Tingay, John Reinecker and Birgit Müller

5.1 Introduction

Borehole breakouts and drilling-induced fractures (DIFs) are important indicators of horizontal stress orientation, particularly in aseismic regions and at intermediate depths (<5 km). Approximately 19 % of the stress orientation indicators in the WSM database have been determined from borehole breakouts and DIFs. Furthermore, borehole breakouts and DIFs provide the majority of stress orientation indicators in petroleum and geothermal systems. Herein we present a broad overview of the procedures for interpreting borehole breakouts and DIFs from image log data and for WSM quality ranking of stress orientations derived from these features.

5.2 Borehole breakouts and drilling-induced tensile fractures

Borehole breakouts are stress-induced enlargements of the wellbore cross-section (Bell and Gough, 1979). When a wellbore is drilled, the material removed from the subsurface is no longer supporting the surrounding rock. As a result, the stresses become concentrated in the surrounding rock (i.e. the wellbore wall). Borehole breakout occurs when the stresses around the borehole exceed that required to cause compressive failure of the borehole wall (Zoback et al., 1985; Bell, 1990). The enlargement of the wellbore is caused by the development of intersecting conjugate shear planes that cause pieces of the borehole wall to spall off (Fig. 5.3-1). The stress concentration around a vertical borehole is greatest in the direction of the minimum horizontal stress (S_h). Hence, the long axes of borehole breakouts are oriented approximately perpendicular to the maximum horizontal compressive stress orientation (S_H; Plumb and Hickman, 1985).

DIFs are created when the stresses concentrated around a borehole exceed that required to cause tensile failure of the wellbore wall (Aadnoy, 1990). DIFs typically develop as narrow sharply defined features that are sub-parallel or slightly inclined to the borehole axis in vertical wells and are generally not associated with significant borehole enlargement in the fracture direction (note that DIFs and breakouts can form at the same depth in orthogonal directions). The stress concentration around a vertical borehole is at a minimum in the S_H direction. Hence, DIFs develop approximately parallel to the S_H orientation (Fig. 5.3-1; Aadnoy and Bell, 1998).

5.3 Introduction to borehole imaging tools

Borehole imaging tools provide an image of the borehole wall that is typically based on physical property contrasts. There are currently a wide variety of imaging tools available, though these predominately fall into two categories: resistivity and acoustic imaging tools.

Resistivity imaging tools provide an image of the wellbore wall based on resistivity contrasts (Ekstrom et al., 1987). Resistivity imaging tools have evolved from dipmeter tools and consist of four- or six-caliper arms with each arm ending with one or two pads containing a number of resistivity buttons. Resistivity image tools provide the same information on borehole diameter and geometry as the older dipmeter tools, however the resistivity buttons also allow high-resolution resistivity images of the borehole wall to be developed (see WSM four-arm caliper log guidelines for a detailed description of dipmeter tools and associated log data). There are a wide variety of wireline resistivity imaging tools available, some of the more common tools are the Formation Micro Scanner

(FMS; from Schlumberger), Formation Micro Imager (FMI; from Schlumberger), Oil-Based Micro Imager (OBMI; from Schlumberger), Simultaneous Acoustic and Resistivity tool (STAR; from Baker Atlas), Electrical Micro Scanner (EMS; from Halliburton) and Electrical Micro Imager (EMI; from Halliburton). Furthermore, recent years have seen the development of a range of logging while drilling (LWD) or measurement while drilling (MWD) resistivity image logging tools, such as the Resistivity At Bit (RAB; from Schlumberger) and STARtrak (from Baker Inteq). For more details on resistivity image logging tools see Ekstrom et al (1987) or Asquith and Krygowski (2004).

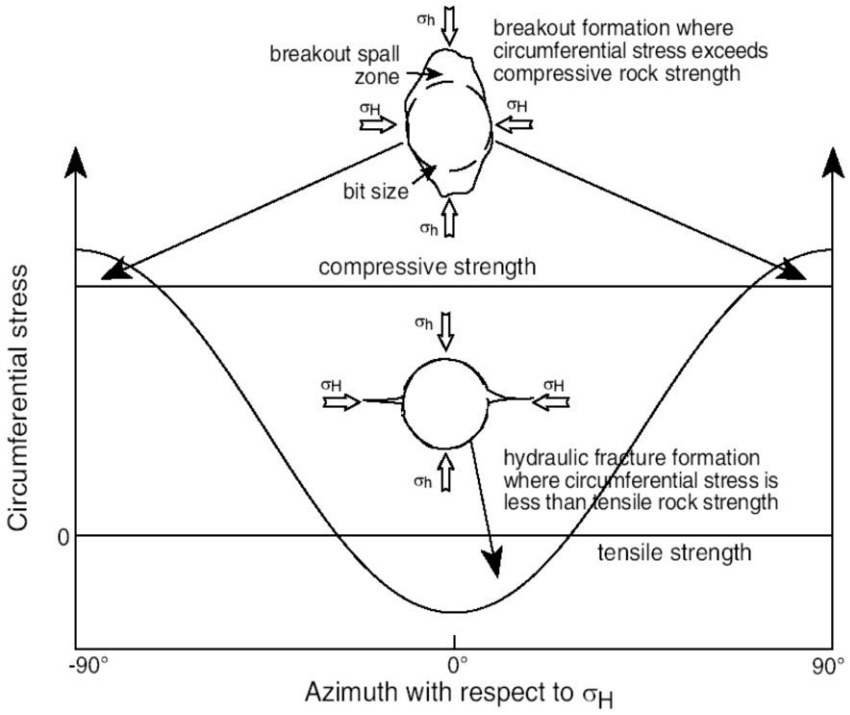

Fig. 5.3-1: Schematic cross-sections of borehole breakout and drilling-induced fracture.

Figure adapted from Hillis and Reynolds, 2000). Borehole breakouts form when the circumferential stress around the wellbore exceeds the compressive rock strength and thus are oriented parallel to the minimum horizontal stress (σ_h). DIFs form when the circumferential stress exceeds the tensile strength of the wellbore wall and are thus oriented parallel to the maximum horizontal stress (σ_H).

Acoustic imaging tools utilise a rapidly rotating piezoelectric transducer to emit a focused high-frequency sonic pulse to the borehole wall (Asquith and Krygowski, 2004). The acoustic imaging tool then records the amplitude of the return echo as well as the total travel time of the sonic pulse. The acoustic wave travel time and reflected amplitude is measured at numerous azimuths inside the wellbore for any given depth. This data is then processed into images of the borehole wall reflectance (based on return echo amplitude) and borehole radius (based on pulse travel time). There are a wide variety of acoustic imaging tools available, some of the more common tools are the Borehole Televiewer (BHTV, from Schlumberger), Ultrasonic Borehole Imager (UBI; from Schlumberger), Circumferential Borehole Imaging Log (CBIL; from Baker Atlas), Simultaneous Acoustic and Resistivity tool (STAR; from Baker Atlas), Circumferential Acoustic Scanning Tool-Visualization (CAST-V; from Halliburton) and the LWD/MWD AcoustiCaliper tool (ACAL; from Halliburton). For more details on acoustic image logging tools see Asquith and Krygowski (2004).

In addition to resistivity and acoustic image logging tools, there are a range of other, currently less common, tools that also provide images of the borehole wall and which may be used for borehole breakout and DIF analysis. Optical image logging tools, such as the Optical Televiewer (from Schlumberger) and Downhole Video tool (from Downhole Video), are wireline tools that utilise cameras to directly image the wellbore wall. Finally, borehole breakouts and DIFs can also be interpreted from MWD/LWD density imaging tools, which provide information on bulk density and photoelectric factor (Pe) at a variety of azimuths around the wellbore and can be used to develop formation density and Pe images. LWD/MWD density image logging tools include the Azimuthal Density Neutron Vision (adnVision; from Schlumberger), Lithotrak (from Baker Inteq) and Azimuthal Lithodensity tool (ALD; from Halliburton).

5.4 Interpreting BOs and DIFs from resistivity image data

Resistivity image logging tools provide the same information of borehole diameter and geometry as the older dipmeter logs and, thus, this data can be used to interpret breakouts in the same way as for four- or six-arm caliper logs (see WSM guidelines on four-arm caliper analysis). However, resistivity imaging logs also provide a high-resolution picture of the wellbore wall based on resistivity contrasts that allows for the direct observation of borehole breakout. Borehole breakout typically appears on resistivity image logs as broad, parallel, poorly resolved conductive zones separated by 180º (i.e. observed on opposite sides of the borehole) and often exhibiting caliper enlargement in the direction of the conductive zones (Fig. 5.5-1; Bell, 1996). Breakouts are typically conductive and poorly resolved because the wellbore fracturing and spalling associated with the breakout results in poor contact between the tool pads and the wellbore wall, which in turn causes the tool to partially or fully measure the resistivity of the electrically conductive drilling mud rather than the formation . However, it is important to note that breakouts will appear as resistive, rather than conductive, zones in resistivity images run in oil-based mud (such as using the OBMI tool).

Drilling-induced fractures can only be observed on image logs. DIFs typically become infiltrated by drilling mud and, thus, appear on resistivity image logs as pairs of narrow, well defined conductive features (resistive in oil-based mud images) separated by 180º (Fig. 5.5-2; Aadnoy and Bell, 1998). Furthermore, unlike natural fractures that tend to cross-cut the wellbore, DIFs are usually aligned sub-parallel or slightly inclined to the borehole axis in vertical wells (Fig. 5.5-3).

5.5 Interpreting BOs and DIFs from acoustic image data

Borehole breakouts are typically interpreted from acoustic image log data using the borehole radius (or travel time) image in combination with images of the reflected amplitude. Borehole breakouts appear as broad zones of increased borehole radius (or travel time) observed on opposite sides of the borehole (Fig. 5.5-3). However, breakouts typically have rough and variable surfaces and thus can also often be observed on reflected amplitude images as broad zones of low amplitude (Fig. 5.5-3).

Drilling-induced fractures are primarily observed on the reflected amplitude image. Both natural and drilling-induced fractures are poor reflectors of acoustic energy. Hence, DIFs appear as narrow zones of low reflectivity separated by 180º and typically sub-parallel or slightly inclined to the borehole axis (Fig. 5.5-3b). DIFs are not commonly associated with any borehole enlargement and thus are often not well exhibited on borehole radius images. However, both natural and drilling-induced fractures may appear on borehole radius images as narrow zones of increased borehole radius (Fig. 5.5-3b).

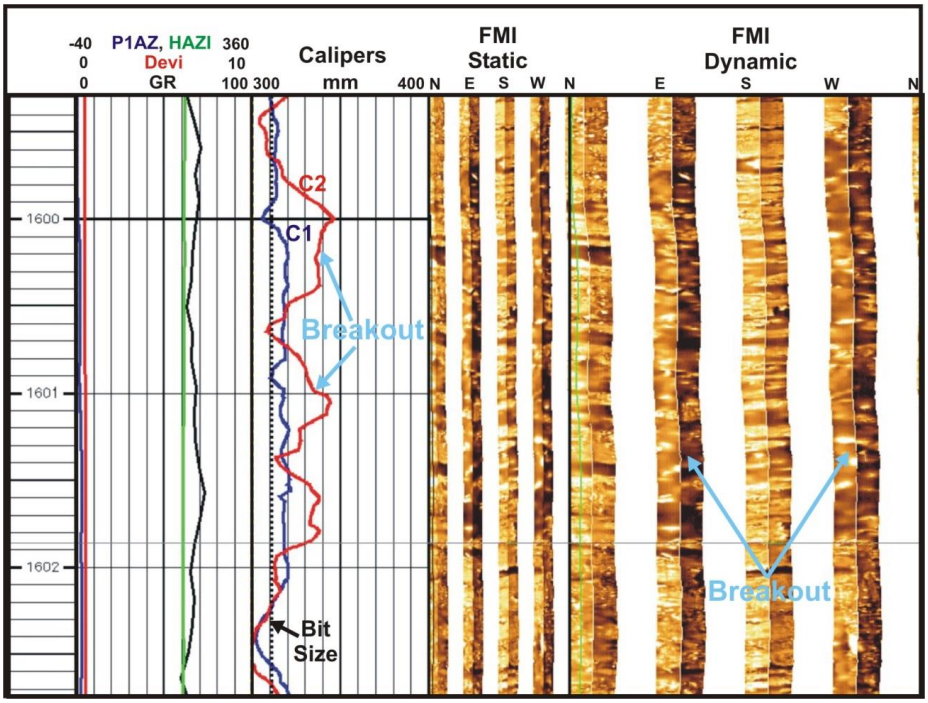

Fig. 5.5-1: Example of BOs interpreted on a Formation Micro Imager (FMI) log.

Breakout is observed both via enlargement in the caliper 2 direction (C2 in red) and directly on the FMI image as broad poorly resolved conductive zones oriented towards 100ºN and 290ºN. These breakouts indicate an approximately N-S maximum horizontal stress orientation.

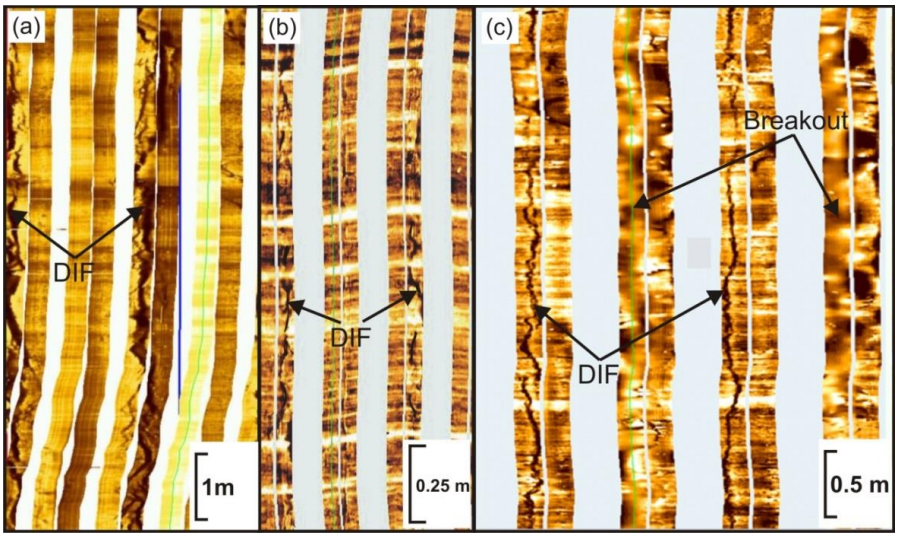

Fig. 5.5-2: Example of DIFs interpreted on Formation Micro Imager (FMI) logs.

DIFs are observed as narrow well defined conductive features separated by 180º and oriented sub-parallel to the borehole axis. (a) DIFs are oriented towards 010ºN and 190ºN, indicating an approximately N-S maximum horizontal stress orientation. (b) DIFs are oriented towards 040ºN and 220ºN, indicating an approximately NE-SW maximum horizontal stress orientation. (c) DIFs are oriented towards 045ºN and 225ºN. Furthermore, breakouts are also observed co-incident with the DIFs. Both the breakouts and DIFs indicate an approximately NE-SW maximum horizontal stress orientation.

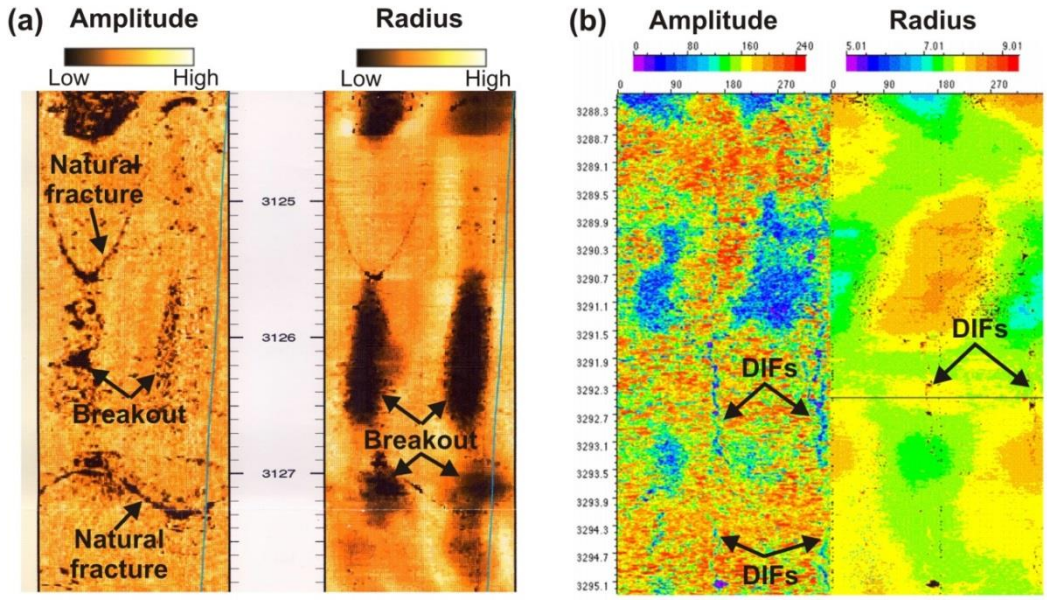

Fig. 5.5-3: Example of BOs and (DIFs observed on acoustic image logs.

(a) BOsd on Ultrasonic Borehole Imager log. BO zones of high borehole radius and, to a lesser extent, low reflection amplitude oriented towards 095-275ºN. The BOs indicate that the present-day maximum horizontal stress is oriented approximately N-S. (b) Borehole Televiewer log showing DIFs oriented towards 165-345ºN. DIFs are observed as zones of low amplitude (left image) and, to a lesser extent, higher radius (right image). The DIFs indicate that the present-day S_{Hmax} is oriented approximately SSE-NNW.

5.6 Interpreting Breakouts and DIFs from Other Image Data

Borehole breakouts and DIFs can also be interpreted from optical image logs and density image logs. On optical image logs (e.g. optical televiewer and Downhole Video), breakouts appear as broad zones of borehole enlargement on opposing sides of the well, while DIFs appear as narrow fractures usually separated by 180º (Fig. 5.6-1). Density imaging logs, like resistivity imaging logs, require the tool to have direct contact with the wellbore wall. Hence, the density imaging tool partially or fully samples the drilling mud rather than the wellbore wall in breakout and DIF zones. Drilling mud is less dense than the formation and hence breakouts appear as broad low density zones separated by 180 degrees (Fig. 5.6-2), while DIFs are sometimes visible as narrow low density axial-parallel fractures on bulk density images. However, many drilling muds also contain barite, which has an extremely high photoelectric absorption factor. Hence, breakouts can also be observed as broad zones of high photoelectric absorption on Pe images (Fig. 5.6-2), while DIFs appear as narrow high Pe fracture zones oriented sub-axial to the wellbore.

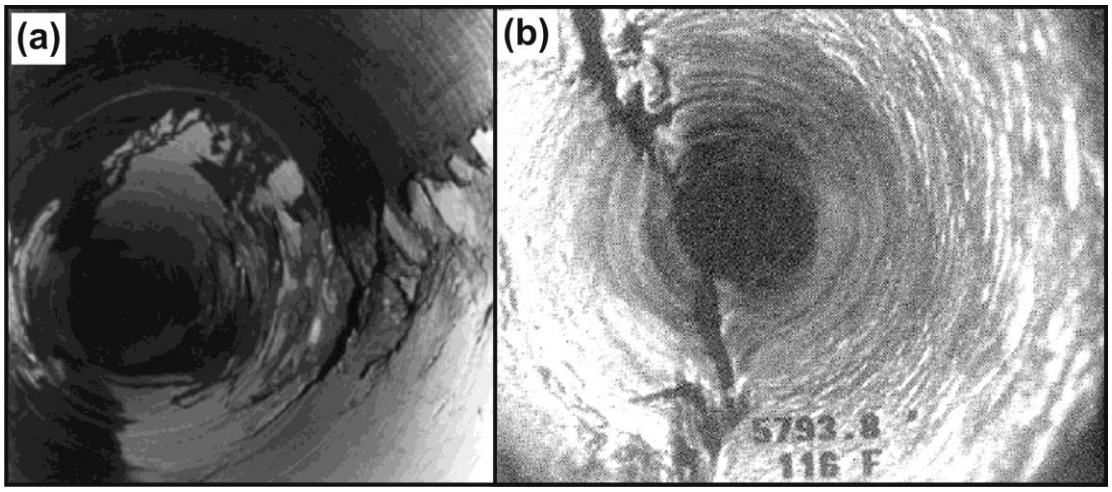

Fig. 5.5-4: Camera images of borehole breakouts.

a) Example of borehole breakout taken by a downhole camera. b) Example of a borehole fracture observed on a downhole camera taken from Asquith and Krygowski (2004).

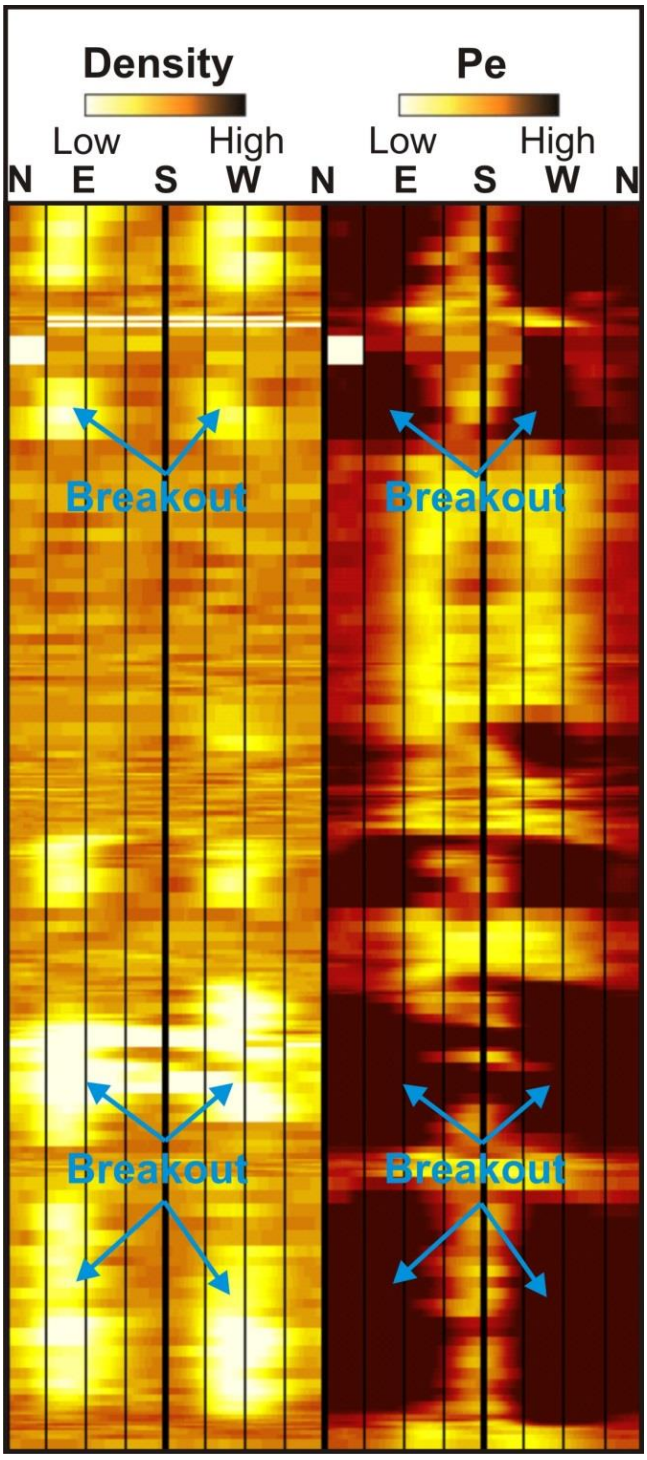

Fig. 5.6-2: Breakout images from a LWD/MWD azimuthal lithodensity tool.

Example of breakouts on density and photoelectric absorption factor (Pe) images from a LWD/MWD Azimuthal Lithodensity tool. Breakouts show up as pairs of broad poorly resolved zones separated by 180º that have low density and high Pe. The breakouts are oriented approximately 060-240ºN and indicate that the present-day maximum horizontal stress is oriented approximately ENE-WSW.

5.7 Determining the mean S_{Hmax} orientation with circular statistics

BO and DIF orientations are bimodal data. Data between 180° and 360° are equivalent to those from the interval 0-180° (S_H varies between 0 and 180°). According to Mardia (1972) the mean breakout azimuth θ_m (i.e. S_h) of a population of n picked breakout long axis directions θ_i is derived by first transforming the angles to the 0-360° interval.

$$\theta_i^* = 2\ \theta_i$$

Then the direction cosine and sine of θ_i^* has to be added and averaged either by the number of measurements (for number weighted mean) or weighted by the BO or DIF length and then divided by the total BO or DIF length L (length weighted mean).

number weighted:

$$C = \frac{1}{n}\sum_{i=1}^{n} \cos\theta_i^*$$

$$S = \frac{1}{n}\sum_{i=1}^{n} \sin\theta_i^*$$

length weighted:

$$L = \sum_{i=1}^{n} l_i$$

$$C = \frac{1}{L}\sum_{i=1}^{n} l_i \cos\theta_i^*$$

$$S = \frac{1}{L}\sum_{i=1}^{n} l_i \sin\theta_i^*$$

where l_i is the length of BO or DIF i with orientation θ_i^*.

The mean azimuth results from: $\theta_m = ½ \arctan(S/C)$

(Make sure that the angles are converted from rad into deg!)

The standard deviation s_o is derived as

$$s_o = 360/2\pi\ (-1/2\ \log_e R)^{1/2} \qquad \text{with} \qquad R = (C^2 + S^2)^{1/2}.$$

5.8 WSM quality criteria for BO and DIF from image logs

All data in the WSM database are quality ranked to facilitate comparison between different indicators of stress orientation (e.g. focal mechanism solutions, overcoring). Image logs provide a much more reliable interpretation of borehole breakouts than four-arm caliper logs. Therefore, stress orientations determined from BO and DIFs interpreted on image log data are quality ranked separately. The quality-ranking criteria are presented in Tab. 5.8.1 and Tab. 5.8-2. Note that BO and DIFs must be treated separately during quality ranking. For example, a well that exhibits both BO and DIFs will receive two stress indicators, one for the stress orientation determined from the BO and another for the stress orientation determined from DIFs.

Tab. 5.8-1: WSM quality criteria for BO data from image logs.
WSM quality ranking criteria for breakouts interpreted from image logs in a single well (s.d. = standard deviation).

A-Quality	B-Quality	C-Quality	D-Quality	E-Quality
≥ 10 distinct breakout zones and combined length ≥ 100 m in a single well with s.d. ≤ 12°	≥ 6 distinct breakout zones and combined length ≥ 40 m in a single well with s.d. ≤ 20°	≥ 4 distinct breakout zones and combined length ≥ 20 m in a single well with s.d. ≤ 25°	< 4 distinct breakout zones or < 20 m combined length with s.d. ≤ 40°	Wells without reliable breakouts or with s.d. > 40°

Tab. 5.8-2: WSM quality criteria for DIF data from image logs.

World Stress Map quality ranking criteria for drilling-induced fractures interpreted from image logs in a single well (s.d. = standard deviation).

A-Quality	B-Quality	C-Quality	D-Quality	E-Quality
≥ 10 distinct DIF zones and combined length ≥ 100 m in a single well with s.d. ≤ 12°	≥ 6 distinct DIF zones and combined length ≥ 40 m in a single well with s.d. ≤ 20°	≥ 4 distinct DIF zones and combined length ≥ 20 m in a single well with s.d. ≤ 25°	< 4 distinct DIF zones or < 20 m combined length with s.d. ≤ 40°	Wells without reliable DIFs or with s.d. > 40°

5.9 References

Aadnoy, B.S. (1990): Inversion technique to determine the in-situ stress field from fracturing data. - J. Petrol. Sci. Engin., **4**, 127-141.

Aadnoy, B.S. and J.S. Bell (1998): Classification of drill-induce fractures and their relationship to in-situ stress directions. - Log Analyst, **39**, 27-42.

Asquith, G. and D. Krygowski (2004): Basic well log analysis. - AAPG Methods in Exploration 16, AAPG, Tulsa, Oklahoma, 244 p.

Bell, J.S. and D.I. Gough (1979): Northeast-southwest compressive stress in Alberta: Evidence from oil wells. - Earth Planet. Sci. Lett., **45**, 475-482.

Bell, J.S. (1990): The stress regime of the Scotian Shelf offshore eastern Canada to 6 kilometres depth and implications for rock mechanics and hydrocarbon migration. - *In:* Maury, V. and D. Fourmaintraux, eds., Rock at Great Depth, Rotterdam, Balkema, 1243-1265.

Bell, J.S. (1996): Petro Geoscience 1. In situ stresses in sedimentary rocks (part 1): measurement techniques. - Geoscience Canada, **23**, 85-100.

Ekstrom, M.P., C.A. Dahan, M.Y. Chen, P.M. Lloyd and D.J. Rossi (1987): Formation imaging with micro-electrical scanning arrays. - Log Analyst, **28**, 294-306.

Hillis, R.R and S.D. Reynolds (2000): The Australian Stress Map. - J. Geol. Soc., London, **157**, 915-921.

Mardia, K.V. (1972): Statistics of directional data: probability and mathematical statistics. - 357 pp., London (Academic Press).

Plumb, R.A. and S.H. Hickman (1985): Stress-induced borehole elongation: A comparison between the Four-Arm Dipmeter and the Borehole Televiewer in the Auburn Geothermal Well. - J. Geophys. Res., **90**, 5513-5521.

Zoback, M.D., D. Moos, L.G. Mastin and R.N. Anderson (1985): Well bore breakouts and in situ stress. - J. Geophys. Res., **90**, 5523-5530.

6 Guidelines for the analysis of overcoring data

John Reinecker, Ove Stephansson and Arno Zang

6.1 Introduction

Overcoring stress analysis (Leeman 1964) belongs to the borehole relief methods (Amadei and Stephansson 1997) and is used for estimating the complete in-situ three-dimensional stress tensor. The main idea behind relief techniques is to isolate partially or wholly a rock sample from the stress field in the surrounding rock mass and monitor its re-equilibrium deformation response. To convert measured strain values to stress requires information of the rock Young's modulus and Poisson's ratio. Details on the different overcoring methods can be found in Amadei and Stephansson (1997), Sjöberg et al. (2003), and Hakala et al. (2003).

Overcoring measurements are common in civil and mining engineering and conducted for design and control of underground openings. The quality of the measurement depends on how the technical problems like drilling, gluing, overcoring are solved and how good the rock characteristics such as anisotropy, discontinuities, and heterogeneity are known (Hakala et al. 2003). Due to technical reasons the measurements are in most cases close to free surfaces (e.g., ground surface, tunnel wall) and are therefore influenced by topography, weathering and excavation activities. However, in most cases the measurements are carried out to gain information on the local state of stress and not for determining the regional tectonic stress field. Therefore, overcoring data are not extensively collected in the WSM.

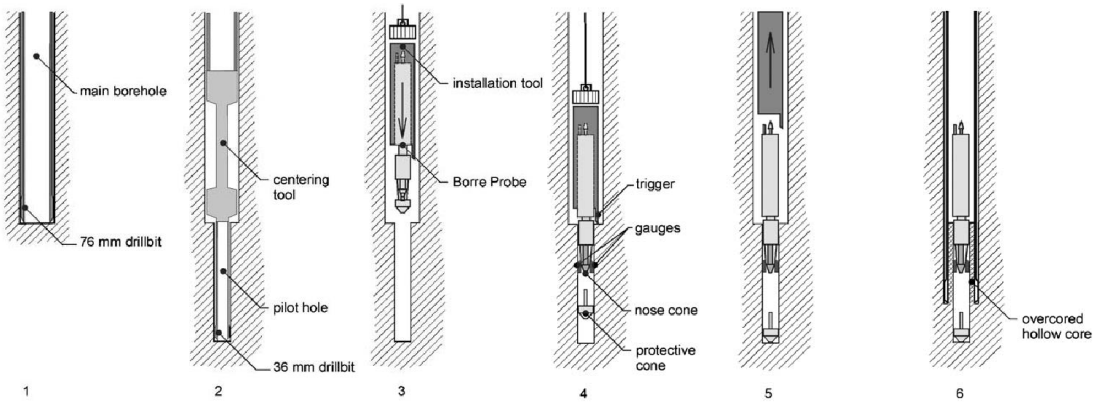

Fig. 6.1-1: Overcoring technique.
General steps in overcoring illustrated by the Borre probe (after Hakala et al., 2003).

There are many variations of overcoring measurements. Borehole relief methods can be subdivided into strain measurements in the borehole wall of shallow holes (e.g., CSIR; Leeman & Hayes, 1966) and in deep boreholes (e.g., USBM (Merrill 1967), CSIRO HI cell (Worotnicki & Walton 1976)). Overcoring strains can be measured at the flat end of the borehole (e.g., Leeman, 1971), at the hemi-spherical end of the borehole (e.g., Sugawara et al., 1986), as well as at the conical end of the borehole (e.g., Kobayashi et al., 1997; Sugawara & Obara, 1995). All strain cells allow determining the 3D state of stress from one single measurement.

Deep doorstopper gauge systems (e.g. Thompson et al., 1997; Thompson & Martino, 2000) allow overcoring measurements at depth as great as 1200 m. Today, on a regular basis in underground projects pilot hole drilling followed by overcoring is used. Then, the doorstopper is the next most

used technique, mainly performed in highly stressed rock when the fracturing is too intense to allow pilot hole drilling (Ljunggren et al., 2003).

6.2 General description of the overcoring technique

Overcoring involves installing a strain-measuring instrument bonded at the bottom of a borehole, or in a small-diameter pilot borehole drilled concentrically at the base of a larger hole. The instrument or cell is then overcored using a larger coring bit, which effectively relieves the stress acting on the hollow rock cylinder (Fig. 6.2-1).

The induced strains are measured by the strain cell before, during, and after overcoring (Fig. 6.2-1). The strain difference are used to back-calculate the stresses acting on the rock cylinder prior to overcoring assuming continuous, homogeneous, isotropic, and linear-elastic rock behaviour. This needs the knowledge of the elastic properties of the rock (Young's modulus and Poisson's ratio), usually determined by biaxial pressure tests on the overcored rock cylinder on-site. Depending on the strain-measuring instrument, either the stresses in the two-dimensional plane orthogonal to the borehole axis, or the complete three-dimensional stress tensor (magnitudes and orientations) at the borehole wall, can then be determined.

Additional to the strain data and rock properties following information are also needed for the interpretation: strain cell temperature while overcoring, water temperature (inflow and outflow), data logger temperature, drill water pressure, drill rotation speed, drill thrust, drill torque, depth of drilling, distance to the next free surface (tunnel, cavern, stope, shaft, borehole, quarry, slope), and distance to tectonic structures. Temperature changes to the rock or strain cell during overcoring have adverse effects on results and therefore it is important to minimize temperature variations (Martino et al. 1997).

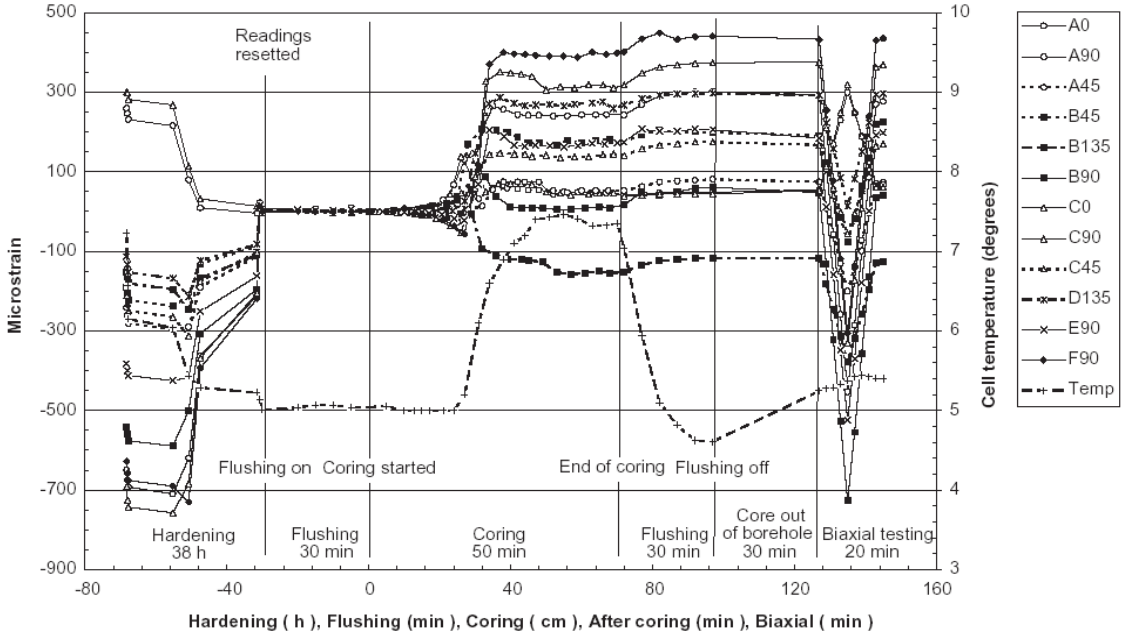

Fig. 6.2-1: Strain measurements measured in overcoring measurements.

Example of measured strains before, during, and after overcoring. Biaxial testing after overcoring is performed to determine the elastic properties of the rock. (Fig. take from Hakala et al., 2003).

6.3 Overcoring data and tectonic stress

Evaluation of rock stress by means of overcoring techniques requires the assumption of ideal rock behaviour: continuous, homogeneous, isotropic, and linear-elastic. Unfortunately these conditions are seldom met completely in rock masses causing errors (accuracy). Even when ideal conditions are met, some scattering of the results always occurs (precision). Amadei and Stephansson (1997) reviewed several studies and found that the expected variability is at least 10-20 %, even in ideal rock conditions. For stress magnitudes an absolute imprecision of at least 1-2 MPa, regardless of stress component or measured value, and an additional relative variability of at least 10 % is reported for overcoring data using the Borre probe (Sjöberg et al. 2003). The variation in orientation is large, particularly for cases when two of the principal stresses are similar in magnitude, usually larger then ±15°.

Different rock structures can affect in-situ stresses at different scales (Amadei and Stephansson 1997). In particular, inclusion of anisotropy due to microcracks associated with unloading of the rock has to be taken into account when analyzing stress measurements at great depth. Rock quality is a major factor when measuring in-situ stresses and large intrinsic errors can be created if the anisotropy is not taken into account. Large structures such as faults can act as in-situ stress domain boundaries and both stress magnitude and orientation can change while crossing those boundaries (Amadei and Stephansson 1997).

The rock volume involved in stress measurements defines the scale of the stress state estimated. With low specimen volumes (e.g. overcoring), the absence and presence of defects is highly variable and stress values can be very different from point to point. As the specimen volume is increased (e.g. borehole breakouts, fault plane solution), the sample of defects becomes more and more statistically representative, until the representative elementary volume (REV) is reached. The REV concept applies to all rock properties, and conditions which are affected by defects, and is especially pertinent for stress data. According to Hudson and Harrison (2000), REV is defined as a volume of rock for which the size of the sample tested contains a sufficient number of defects for the “average” value of stress to be reasonably consistent with repeating testing. The far-field in situ stress (super-REV stress) is the one which we would require for the tectonic stress field. In the design of underground excavation, however, a local near-field structural stress value due to defects acting on small rock volumes (sub-REV stress) may be critical for the stability of the structure as a whole, and worth to measure.

For regional tectonic stresses Zoback and Zoback (1991) claim a variety of non-tectonic processes affecting in-situ stresses near Earth's surface to dominate stress data from overcoring measurements. Because it is very hard to proof the tectonic origin of the measured stress, overcoring data in depths less than 100 m are not believed to be reliably indicative of the regional stress field at midcrustal depths. Therefore, shallow overcoring stress data are given a comparably low quality even if the quality of the measurement itself is exellent.

6.4 WSM quality criteria for OC data

All data in the WSM database are quality ranked to facilitate comparison between different indicators of stress orientation (e.g. focal mechanism solutions, drilling-induced tensile fractures, overcoring). The quality ranking criteria for stress orientations determined from overcoring stress measurement is presented in Tab. 6.4-1.

Tab. 6.4-1: WSM quality criteria for OC data.

WSM quality ranking criteria for overcoring stress measurements (s.d.=standard deviation).

A-Quality	B-Quality	C-Quality	D-Quality	E-Quality
• ≥ 11 measurements with depth ≥ 300 m and s.d. ≤ 12°	• ≥ 8 measurements with depth ≥ 100 m and s.d. ≤ 20°	• ≥ 5 measurements with depth ≥ 30 m and s.d. ≤ 25°	• ≥ 2 measurements with depth ≥ 10 m and s.d. ≤ 40°	• < 2 measurements or depth < 10 m or s.d. > 40° • Measurements in boreholes extending less than two excavation radii from the excavation wall • Distance to topographic features less than three times the height of the topographic feature

6.5 References

Amadei, B. and O. Stephansson (1997): Rock stress and its measurement. - 490 pp., Chapman & Hall (London).

Hakala, M., J. A. Hudson, and R. Christiansson (2003): Quality control of overcoring stress measurement data. - Int. J. Rock Mech. Min. Sci., **40**, 1141-1159.

Hudson, J. A. and J. P. Harrison (2000): Engineering rock mechanics. - 456 pp., Elsevier (Oxford).

Kobayashi S., T. Yamaguchi, and T. Yoshikawa (1997): Initial stress estimation in rock using ultrasonic. - In: Proceedings of the International Symposium Rock Stress, Japan, Sugawara, K. and Y. Obara (eds), AA Balkema, Rotterdam, pp 161-166.

Leeman, E. R. (1964): The measurement of stress in rock – Parts I, II and III. - J. South Afr. Inst. Min. Metall., **65**, 45-114 and 254-284.

Leeman, E. R. and D. J. Hayes (1966): A technique for determining the complete state of stress in rock using a single borehole. - In: Proceedings 1st Congress International Society of Rock Mechanics, Lisbon, Volume 2, pp. 17-24.

Ljunggren, C., Y. Chang, T. Janson, and R. Christiansson (2003): An overview of rock stress measurement methods. -Int. J. Rock Mech. Min. Sci., **40**, 975-989.

Martino, J. B., P. M. Thompson, N. A. Chandler, and R. S. Read (1997): The in situ stress program at AECL's Underground Research Laboratory, 15 years of research (1982-1997). - 100 pp., NWMD, Ontario Hydro, Canada.

Merrill, R. H. (1967): Three component borehole deformation gage for determining the stress in rock. - US Bureau of Mines Report of Investigation RI 7015.

Sjöberg, J., R. Christiansson, J. A. Hudson (2003): ISRM Suggested Methods for rock stress estimation ─ Part 2: overcoring methods. - Int. J. Rock Mech. Min. Sci., **40**, 999-1010.

Sugawara, K., Y. Obara, K. Kaneko, T. Aoki (1986): Hemispherical-ended borehole technique for measurement of absolute rock stress. - In: O Stephansson (ed), Rock Stress and Rock Stress Measurements, Centek Publishers, Lulea, Sweden, pp. 207-216.

Sugawara, K. and Y. Obara (1995): Rock stress and rock stress measurements in Japan. - In: Proceedings International Workshop on Rock Stress Measurement at Great Depth, Tokyo, Japan, pp. 1-8.

Thompson, P. M., R. Corthesy, and M. H. Leite (1997): Rock stress measurements at great depth using the modified doorstopper gauge. - In: Proceedings of the International Symposium Rock Stress, Japan, Sugawara K & Obara Y (eds), AA Balkema, Rotterdam, pp. 59-64.

Thompson, P. M. and J. Martino (2000): Application of the Doorstopper gauge system to deep in situ rock stress determinations. - Report No. 06819-REP-01200-10019-R00, Atomic Energy of Canada Limited.

Worotnicki, G. and R. J. Walton (1976): Triaxial hollow inclusion gauges for determination of rock stresses in-situ. - In: Supplement to Proceedings ISRM Symposium on Investigation of Stress in Rock, Advances in Stress Measurement, Sydney, The Institution of Engineers, Australia, Suppl. pp. 1-8.

Zoback M. D. and M. L. Zoback (1991): Tectonic stress field of North America and relative plate motions. - In: The Geology of North America, Decade Map Vol. 1, Neotectonics of North America. Geological Society of America, Boulder, pp. 339-366.

7 WSM database format description

7.1 Introduction

Note that only the fields ISO, LAT, LON, AZI, TYPE, DEPTH, Qualtiy, regime country are needed to plot the stress data record with the online WSM database interface CASMO. All other fields present individual additional information for the data records.

7.2 Database field format description

Table 6.2-1 describes the details of the fields given for each data record in the WSM database release 2016 in sequential order of appearance. The first column one gives the field name used in the database file, the second column gives an example how an entry might look like, the third column indicates for which type of stress indicator this field is applied, the fourth column gives a detailed description, and the fifth column states the range of possible values for the field. The 57 fields are listed in the sequential order as they occur in the database file for each data record.

Tab. 7.2-1: Explanation of fields for each data record.
The table explains the each field of each data records in sequential order of appearance.

Field	Example	Used For	Explanation	Range
ISO	WSM3243	ALL	Data record identification code. ISO is given by the WSM team and is a serial number.	
SITE	EG 13	ALL	Site code as e.g given in publications and reports.	
LAT	46.533	ALL	Latitude (South latitude is negative)	-90° - +90°
LON	-119.682	ALL	Longitude (West longitude is negative)	-180° - +180°
AZI	45	ALL	Orientation of the maximum horizontal stress S_{Hmax} in degrees (clockwise from North)	0° - 180°
TYPE	FMS	FM*	Earthquake focal mechanisms: FMF: formal inversion of several focal mechanisms FMS: single focal mechanism solution FMA: average of p-axis or composite focal mechanism soluations	FMF FMS FMA
		BO*	Borehole breakouts: BO: from analysis of individual breakouts BOC: from analysis or cross-sectional shape of entire well BOT: from televiewer-imaged shapes of individual breakouts	BO BOC BOT

		HF*	Hydraulic fracturing measurement: HF: with no magnitude information HFG: magnitude reported as gradient HFM: magnitude reported for maximum depth HFP: testing of pre-existing fractures (HTPF technique) stress magnitudes from inversion of tests over a depth interval	HF HFG HFM HFP
		OC	OC: overcoring or other strain relief measurement	OC
		GF*	Geologic fault-slip data: GFI: inversion of fault-slip data observed on planes of a variety of trends GFM: paleo-focal mechanism, P-axis measured at 30° to fault in plane of slip vector GFS: orientation from fault attitude and primary sense of offset	GFI GFM GFS
		GVA	GVA: geologic-volcanic vent alignment	GVA
		PC	PC: petal centerline fracture, orientation from mean orientation of petal fractures in oriented core	PC
		SR	SR: strain recovery method; also called wave velocity anisotropy, currently not considered as a reliable stress indicator (available results included as E-quality)	SR
		SW*	SW: shear wave splitting, currently not considered as a reliable stress indicator (available results included as E-quality). SWB – Shear Wave Splitting in Boreholes SWL – Shear Wave Splitting in Laboratory SWS – Shear Wave Splitting in Seismology	SWB SWL SWS
		DIF	DIF: drilling-induced tensile fractures of the borehole wall	DIF
		BS	BS: borehole slotter	BS
DEPTH	1.9	ALL	Depth of measurement or mean depth, e.g. for breakouts in a well [km]	0 - 40
QUALITY	B	ALL	According to WSM Quality Ranking Scheme. Only qualities A-C are considered as reliable stress indicators	A,B,C,D,E
REGIME	TF	ALL	Stress regime defined in the following manner: TF: thrust faulting $S_{Hmax} > S_{hmin} > S_V$ TS: thrust with strike-slip component SS: strike-slip $S_{Hmax} > S_V > S_{hmin}$ NS: normal with strike-slip component NF: normal faulting $S_V > S_{Hmax} > S_{hmin}$ U: unknown stress regime	TF TS SS NS NF U

LOCALITY	R-142	ALL	Name of location or well	
COUNTRY	GERMANY	ALL	The country name according to the listing of the United Nations list.	
DATE	19911223	FM*	Date of earthquake (year month day)	
		BO*	Date of measurement (year month day)	
TIME	03:15:38.2	FM*	Time of earthquake occurrence (UT). If time is given less accurately, please use x at the appropriate digit position (e.g. 16:45:xx.x)	
NUMBER	21	FMF,FMA	Number of focal mechanisms analyzed in inversion, average or composite solutions	
		BO*, HF*, OC*, GF*	Number of orientation observations	
		PC	Number of fractures	
		GVA	Number of volcanic vent alignments	
		DIF	Number of drilling-induced fracs	
SD	17	FMA, FMF, BO, HF, OC, DIF, GF*, GVA, PC	Standard deviation of orientations	0° - 90°
METHOD	MI	FM*	Method used to determine mechanism (blank unless any of the below apply) FM: for first motions MI: for moment tensor inversion AR: for amplitude ratio	FM MI AR
		OC	Method of strain relief measuring technique (blank unless any of the below apply) FJ: Flat jack DS: Doorstopper TR: Triaxial cell	FJ DS TR
S1AZ	28	FM*, HF*, OC, GF*	Azimuth (clockwise from N) of P-axis	0° - 360°
S1PL	85	FM*, HF*, OC, GF*	Plunge (from horiz.) of P-axis	0° - 90°
S2AZ	108	FM*, HF*, OC, GF*	Azimuth of B-axis	0° - 360°
S2PL	10	FM*, HF*, OC, GF*	Plunge of B-axis	0° - 90°
S3AZ	10	FM*, HF*, OC, GF*	Azimuth of T-axis	0° - 360°

S3PL	5	FM*, HF*, OC, GF*	Plunge of T-axis	0° - 90°
MAG_INT_S1	80	HFM, HFG	HFM: maximum magnitude (at greatest depth) in [MPa], or HFG: intercept in [MPa]	
		OC	Maximum magnitude (at greatest depth) in [MPa], or intercept in [MPa]	
			Note: negative stress magnitudes indicate tension	
SLOPES1		HFG	Slope [MPa/km]	
MAG_INT_S2	60	HFM, HFG, OC	Equivalent to MAG_INT_S1	
SLOPES2		HFG	Equivalent to SLOPES1	
MAG_INT_S3	54	HFM, HFG, OC	Equivalent to MAG_INT_S1	
SLOPES3		HFG	Equivalent to SLOPES1	
PORE_MAGIN	20	HFM, HFG, OC	Pore pressure magnitude (at greatest depth) in [MPa], or intercept in [MPa]	
PORE_SLOPE		HFG	Pore pressure slope [MPa/km]	
MAG_TYPE	Mw	FMF, FMS, FMA	Type of magnitude determination (of strongest event for FMF or FMA) mb: body-wave magnitude ML: local magnitude Ms: surface-wave magnitude Mw: moment magnitude	mb ML Ms Mw
EQ_MAGN	5.1	FMF, FMS, FMA	Magnitude (of strongest event for FMF or FMA)	
MOM	5.0	FMS	Mantissa of seismic moment	
MOM_EXP	23	FMS	Exponent of seismic moment [dyne cm]	
EQ_AVG	G	FMA	Averaging method used for groups of focal mechanisms: G: geometric average from stereoplot of P- and T-axes C: composite, i.e. average of p-axis of several single focal mechanisms	G A
TOT_LEN	350	BO*	Total length of breakouts in a well [m]	
		GVA	Total length of volcanic alignments [m]	
		DIF	Total length of drilling induced fracs [m]	
SD_WEIGHT	L	BO*, HF*, OC, GF*,	Weighting method used for std. deviation: L= length, N= number	L N

		GVA, PC, DIF		
SAMP_INT	.03	BO*	Sample interval [m] of measurements	
TOP	1500	BO*	Top of breakout interval [m], please enter top of measurement interval in comments	
		HF*	Top of interval of hydrofrac measurements [m]	
		DIF	Top of drilling induced frac interval [m]	
BOT	2800	BO*	Bottom of breakout interval [m], please enter bottom of measurement interval in comments	
		HF*	Bottom of interval of hydrofrac measurements [m]	
		DIF	Bottom of drilling induced frac interval [m]	
NO_MAG_VEN	7	HF*	Number of magnitude measurements	
		GVA	Total number of volcanic vents	
YOUNG	25	OC, GF*	Young's modulus (GPa)	
POISSON	0.24	OC, GF*	Poisson's ratio	
ROCK	granite	HF*, OC, GF*, GVA, PC	Rock type	
AGE	Quaternary	OC	Age of rock	
		GF*	Age of geological slip occurence	
		GVA	Age of volcanic eruption	
RATIO	0.3	FMF, GFI	Relative stress magnitude ratio R=(S2-S3)/(S1-S3) from: FMF: formal inversion of several single earthquake focal mechanisms GFI: fault-slip inversion from geological data	0....1
DIPAZ		GFS	Dip azimuth of fault plane when only primary sense of offset is known	
DIP		GFS	Dip of fault plane when only primary sense of offset is known	
REF1	ZOBAXX1990A	ALL	First four letters of first author's surname, +first two letters of the second author's surname (use XX if no second author) +year +sequence letter to avoid duplicate ref-codes for different references!	
REF2		ALL	See REF1	
REF3		ALL	See REF1	

REF4		ALL	See REF1	
COMMENT	Coordinates read from the maps	ALL	These comments can be used for noting possible errors with data or conflicting results with some indication of why the particular result was used. The comments can also be used to indicate the number or name of this solution or result in a particular reference, e.g. BELLPO1985#41W-371 would indicate well number #41W-371 in a Bell and Podrouzky (1985) paper, or the time of occurrence of an earthquake (GMT). Use NC if there are no additional comments.	
LAST_MOD	20010730	ALL	Date of the last modification of this database entry. Leave empty (will be entered by the WSM team).	
DIST	234	ALL	Distance in [km] of the stress data point to the nearest plate boundary of the global plate model PB2002 from Bird (2003).	
BOUNDARY	OTF	ALL	Type of plate boundary according to the global plate model PB2002 from Bird (2003): CTF=Continental Transform Fault CRB=Continental Rift Boundary CCB=Continental Collision Boundary OTF=Oceanic Transform Fault OSR=Oceanic Spreading Ridge OCB=Oceanic Collision Boundary SUB=Subdcution zone	
PBE	PBE	FMS	Stands for 'Possible Plate Boundary Event'.	PBE NO